A Three-Dimensional Model of Geoelectric Structure
in the Northern Coast Ranges, California
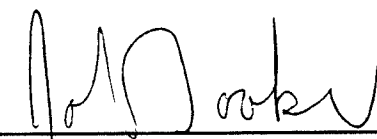
by

Maryann G. Helferty

A thesis submitted in partial fulfillment
of the requirements for the degree of

Master of Science

University of Washington

1989

Approved by _____
(Chairperson of Supervisory Committee)

Program Authorized
to Offer Degree_____ _Geophysics Program_____

Date_____ _5/26/89_____

Master's Thesis

In presenting this thesis in partial fulfillment of the requirements for the Master's degree at the University of Washington, I agree that the Library shall make its copies freely available for inspection. I further agree that extensive copying of this thesis is allowable only for scholarly purposes, consistent with "fair use" as perscribed in the U.S. Copyright Law. Any other reproduction for any purposes or by any means shall not be allowed without my permission.

Signature _Maryann Hilferty_

Date _6/7/89_

The most convincing model to explain the numerous geothermal centers in the North-
ern Coast Ranges is that of a buried half-spreading center. This thesis reports on the
search for a conductivity anomaly associated with the asthenospheric window bounded by
the southern edge of the subducted Gorda plate. If the strong field contribution from the
coast effect can be subdued with a source polarization along strike with the average coast-
line, then a buried plate edge would produce a single peak in anomalous magnetic fields, Z,
centered over the step. An array of 18 magnetometers was deployed in 1986 as part of this
field experiment. Induction arrows and a hypothetical event analysis for the array are
presented along with an interpretation of the geoelectric structure of the Cape Mendocino
region.

The data analysis show that a two-dimensional interpretation does not suffice to
explain the observed anomalous magnetic fields. Specifically, the azimuth of the real induc-
tion arrows changes with period and the real and imaginary arrows are not co-planar. A
north-south profile of observed Z values is compared against a two-dimensional model of a
step in the aesthenosphere and the following differences are noted: (a) model values of
Real(Z) are always positive in contrast to the large negative values observed at both ends
of the profile, (b) model values of Real(Z) are less frequency dependent than the observed
fields, (c) model values of Imag(Z) are symetric about the step whereas observed values
continuously increase to the south. The observed fields are strong and attest to a compli-
cated geoelectric structure along the continental margin.

Surface conductive features could contribute to the anomalous fields recorded by the
array and complicate the choice of a source polarization that best delineates deeper struc-
ture. I developed a three-dimensional model of the surface geology and bathymetry for the
study area. Using thinsheet modelling programs at the San Diego Supercomputer Center, I
calculated the anomalous fields produced by the irregular coastline, the metasediments of
the Coast Ranges, and the northern terminus of the Sacramento Valley. The caluclations
demonstrate that the magnetometer array is strongly influenced by these surface conductors
which impede the search for a conductivity anomaly associated with the Gorda Plate edge.

Table of Contents

List of Figures

List of Tables

Acknowledgements

CHAPTER 1

INTRODUCTION

1.1 Geologic Setting

The Mendocino Triple Junction marks the northwest end of the San Andreas transform and thus also the northwest corner of a hypothesized window in the subducted slab beneath western North America (Figure 1.1.1) (Dickinson and Snyder, 1979). This slab window is bounded on the north by the southern edge of the subducted Gorda Plate and extends east to the Rockies. In this triangular hole, asthenosphere is present at shallow depths. The myriad of geothermal areas of northern California, including the Geysers and Clear Lake regions, attest to the presence of shallow asthenosphere under the Coast Range south of Cape Mendocino. Indeed, the most convincing model to explain the thermal structure of the Coast Range involves a half spreading center beneath the North American lithosphere at the southern edge of the Gorda Plate (Lachenbruch and Sass, 1980). To an observer on the Pacific Plate, the North American continent slides southward over the subducting Gorda Plate, at a rate of 50 km/My. As the continental lithosphere slides off the southern edge of the subducted Gorda plate, it comes in contact with deeper, nonsubducting material on the east side of the San Andreas Fault, which it then proceeds to drag southward (Figure 1.1.2). Mass is conserved by upwelling of deeper asthenospheric material just south of the edge of the Gorda plate. Partial melting of the rising material and of the lower lithosphere in contact with it produces the magmas for the geothermal areas; diffusion of the heat up into the lithosphere on a larger scale accounts for the elevated heat flow values observed in the southern Coast Range.

Both Dickinson and Snyder, as well as Lachenbruch and Sass, assumed that the southern edge of the Gorda Plate would parallel the Mendocino Fracture Zone (MFZ). However, Jachens and Griscom (1983) have used an isostatic reduction of the gravity field to infer that the plate edge is actually parallel to the Blanco Fracture Zone and proceeds southeastwards at least 100 km from Cape Mendocino. There the gravity data suggest that the plate edge bends parallel to the MFZ and proceeds eastward under the Great Valley. The sense of the gravity anomaly (higher values to the south) supports the presence of asthenosphere juxtaposed

against lighter subducted Gorda Plate. The trajectory of the anomaly implies that the Gorda Plate is presently deforming around the corner of the Pacific Plate under Cape Mendocino and that the overall spreading direction of the Juan de Fuca-Gorda Plate changed from being parallel to the MFZ to its present direction at about 4 ma.

The gravity signature of the plate edge is a rather subtle effect. A buried half spreading center should produce a much larger anomaly in electrical properties. This thesis reports initial results of an experiment to detect and delineate the electrical anomaly. The signals observed are time-varying magnetic fields due to magnetospheric-ionospheric disturbances. These fields diffuse into the' earth where two and three-dimensional earth structure produce anomalous vertical fields which can be mapped by an array of magnetometers.

1.2 Organization of This Thesis

This thesis will present results of the field experiment and three numerical models used to interpret the magnetic fields observed by the array. Chapter 2 introduces the theory of geomagnetic depth sounding and Chapter 3 describes the design of the field experiment. The problem of anomalous fields resulting from surface conductors is discussed in Chapter 4 along with the numerical model and solution method used to estimate their contribution to the observed Z values. Next, the anomalous magnetic fields observed by the array are presented both as induction arrows and in hypothetical event analyses in Chapter 5. The chapter closes with the presentation of results from the three-dimensional model and interpretation of the data. Chapter 6 presents the conclusions drawn from a comparison of a N - S profile of the array with a two-dimensional model of a step in the asthenosphere.
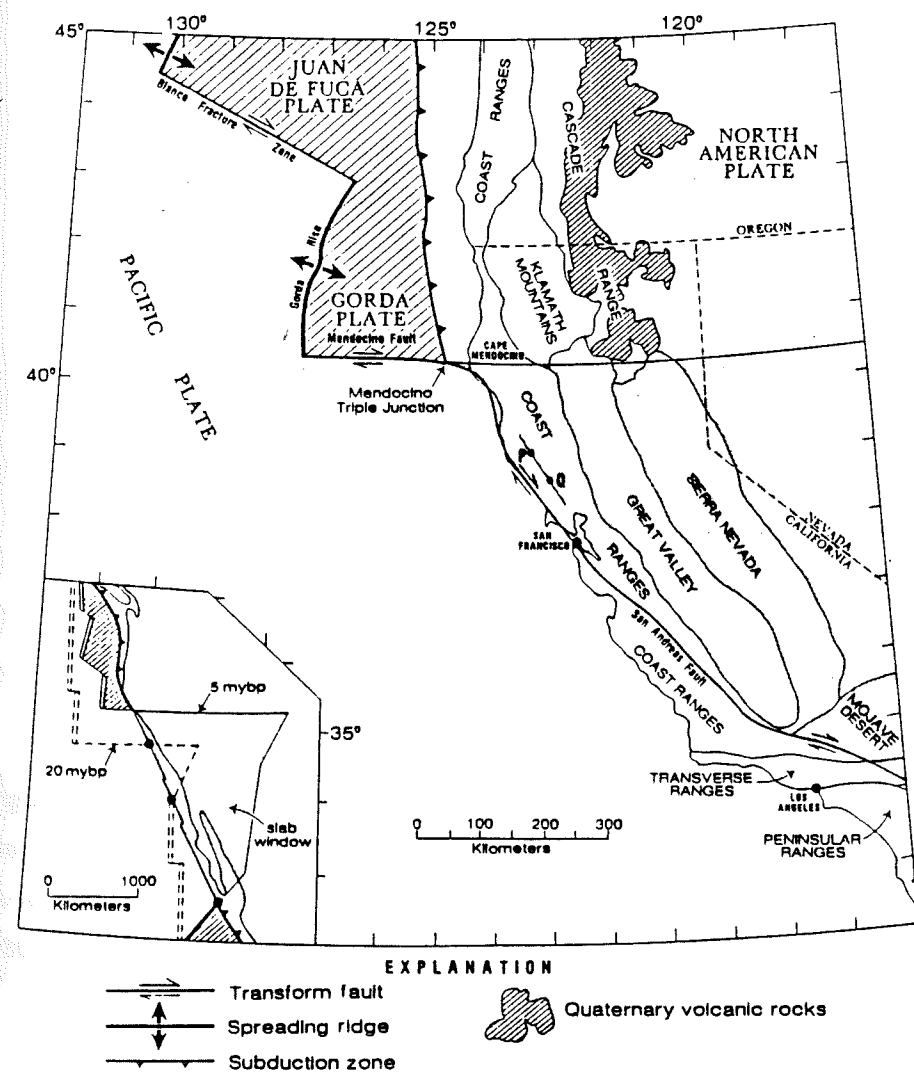
Figure 1.1.1 Index map showing major lithospheric plates, plate boundaries, and provinces near the west coast of California and Oregon (after *Jachens and Griscom*, 1983). The Gorda plate is a subplate of the Juan de Fuca plate system. Distribution of Quaternary volcanic rocks of the Cascade Range is after *Blakely and Christiansen* (1978). Shaded area shows hypothesized location of window in subducted slab, and inset map shows two stages in the development of the slab window (after *Dickinson and Snyder*, 1979).
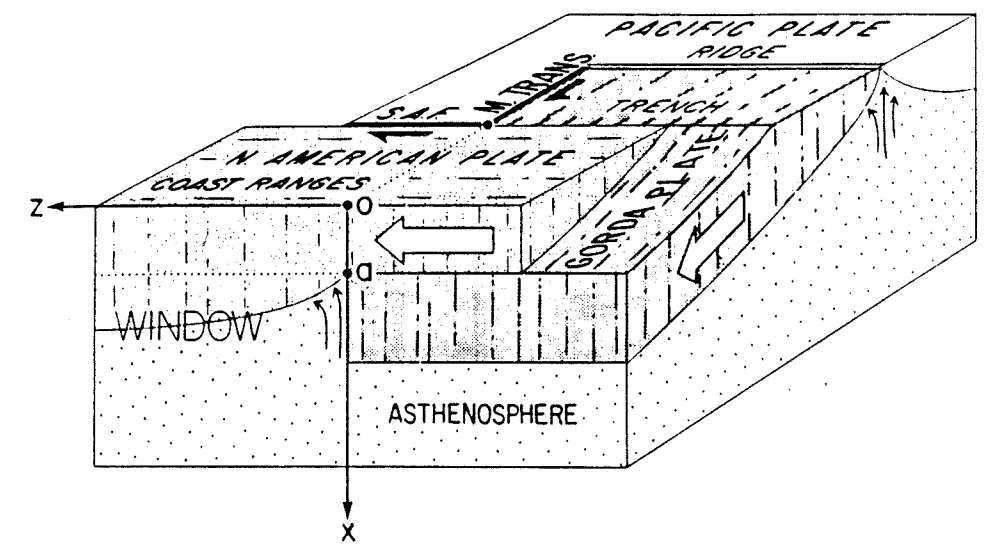
Figure 1.1.2 Idealized relations among tectonic plates near the Mendocino Triple Junction (intersection of the Mendocino transform (M. Trans.) and the San Andreas fault (S.A.F.)). Arrows indicate motion relative to a fixed Pacific plate. (Figure after *Lachenbruch and Sass*, 1980)

CHAPTER 2

Theory of Geomagnetic Induction

Electrical methods are used to determine the conductivity structure of the earth. With this information, geophysicists can constrain models of the thermal regime and chemical composition of the earth's interior. The basic physics of this experiment is the diffusion of electromagnetic fields into the lithosphere. This section presents the theory of geomagnetic induction for planar structures. Section 2.1 discusses application of Maxwell's equation to diffusion of magnetic fields in a one-dimensional earth. Section 2.2 presents theory for the transfer functions used to locate anomalous geoelectric structure in the earth.

2.1 Diffusion of Magnetic Fields in Conductors

The problem of electromagnetic induction within the earth falls into the broad class of physical problems described by Maxwell's equations. This section introduces the phenomenon of diffusion of EM fields into the earth and defines the important parameters of this process such as skin depth and diffusion wavelength. To describe the problem mathematically let E and H represent the intensities of the electric and magnetic fields. Then their spatial and temporal variation are described by:

$$\nabla \times E = \frac{-\partial B}{\partial t} \qquad \nabla \cdot D = \rho \tag{1}$$

$$\nabla \times H = \frac{+\partial D}{\partial t} + J \quad \nabla \cdot B = 0 \tag{2}$$

and

$$J = \sigma E$$

in this formulation D and B represent the electric and magnetic flux densities. In a linear isotropic media, the field intensities and flow densities are related by the constitutive relations:

$$D = \varepsilon E$$

$$B = \mu H$$

When induction is studied in a geophysical context then further simplifying assumptions are made, based upon the characteristic physical properties of earth materials. Taking the curl of equation 2 and substituting from equation 1 yields:

$$\nabla^2 H = \mu \left[\sigma \frac{\partial H}{\partial t} + \varepsilon \frac{\partial^2 H}{\partial t} \right] \qquad H = (x, y, z, t)$$

The result is a wave equation known as the Helmholtz equation which describes the propagation of time varying magnetic fields into a conductor. The Fourier transform of this equation with exp (+iωt) time dependency yields

$$(\nabla^2 + k^2) \, H \, (x \, y \, z, \, \omega) = 0$$

where k is the propagation constant in the medium

$$k = [-i\sigma\mu\omega + \varepsilon\omega^2 t]^{\frac{1}{2}}$$

In the earth, $\sigma \mu \gg \omega\varepsilon$ and the quasistatic approximation simplifies to

$$k = [-i\sigma\mu\omega]^{\frac{1}{2}} = \pm \frac{1 + i}{2} (\sigma\mu\omega)^{\frac{1}{2}}$$

Numerous formal solution methods are available to obtain the fields to be observed in a conducting medium.

Commonly it is assumed that the source field is a vertically incident plane wave. For a layered earth this requires that the incident E and H fields are perpendicular and can only vary in the z direction. In a one-dimensional earth, the Helmholtz equation simplifies to an ODE. The sign of z is taken as positive downwards into the earth. Consequently the attenuation of the magnetic field energy into heat in the earth requires the selection of the positive square root of k. A damped exponential solution has the form:

$$H = H_0 \, e^{-z/\delta} e^{-i(\omega t - \frac{z}{\delta})}$$

where $\delta = (2/\text{sigma}\mu\omega)^{\frac{1}{2}}$ is the skin depth of penetration of fields in the medium. Thus the magnetic field which propagates into the earth has a depth dependent attenuation as well as a depth dependent phase shift.

This motivates the definition of another common induction parameter known as the diffusion wavelength, λ. It characterizes the distance $\lambda=2\pi\delta$ required for the phase of the diffusing magnetic field to rotate through 2π. The current induced at a given depth, z, from a magnetic field oriented along the y axis is:

$$\nabla \times H = \sigma E = J$$

$$J_x = \frac{-\partial H_y}{\partial z} = -\frac{\partial}{\partial z}\left[H_0\,e^{\frac{-z}{\delta}}\exp(\omega t - \frac{z}{\delta})\right]$$

$$J_x = \sqrt{\omega\mu\sigma}H_0\,e^{\frac{-z}{\delta}}\exp(\omega t - \frac{z}{\delta}+\frac{\pi}{4})$$

This skin effect distributes current in a frequency dependent fashion throughout a conducting medium.

The secondary magnetic fields produced by this induced current is easily calculated from Ampere's Law:

$$H_y = \frac{J_x}{z}\hat{y}$$

After this secondary magnetic field diffuses back to the surface the net phase shift is $-2z/\delta + \pi/4$ for a sheet current at depth z. The same phase will result from a sheet current at depths that are multiples of $z=\pi\delta$. This ambiguity of the phase constrains our ability to determine vertical conductivity structure from GDS data. Even in the simple case of a layered half-space, measurements of the magnetic fields at the surface can only constrain the conductance of structure below. Consequently, in field experiments over complicated geoelectric structure, GDS studies are commonly used solely to define lateral changes in conductivity.

2.2 Transfer Functions

This section describes the calculation of transfer functions and their use in the interpretation of GDS data. In the earth, lateral variations in conductivity will affect the vertical magnetic fields recorded at a station. The correlation between a horizontal and vertical field components can form a transfer function; such quantities can be represented in induction arrows which denote the magnitude and phase of correlation between the two components. As the period of the sounding increases, then image currents will flow deeper within the earth. The magnitude and direction of the induction arrows calculated from the transfer

functions will change as the conductivity structure at depth changes.

The sources for GDS experiments are the ionospheric currents that produce magnetic fields. At mid-latitude, these fields can be considered uniform on a scale of 10,000 km (Banks, 1973). The three components of the magnetic field will henceforth be denoted by $H = (X, Y, Z)$. When these fields diffuse into earth, a vertical magnetic field is produced at the surface. Often the total field, Z_t is divided into two components. The normal field Z_n is that contributed by the "regional" structure; ideally, this resembles a one dimensional layered subspace. The anomalous field Z_a is that produced by local inhomogeneities - usually the geologic targets of interest.

$$Z_T = Z_N + Z_A$$

In the experiment we measure the total vertical field but for the data analysis we assume that any vertical fields are entirely anomalous. The vertical fields are correlated with the horizontal components through a transfer function:

$$\begin{array}{l} X = \\ Y = \\ Z = \end{array} \begin{bmatrix} T_{xx} & T_{xy} & T_{xz} \\ T_{yx} & T_{yy} & T_{yz} \\ T_{zx} & T_{zy} & T_{zz} \end{bmatrix} \begin{bmatrix} X_n \\ Y_n \\ Z_n \end{bmatrix} + \begin{bmatrix} e_x \\ e_y \\ e_z \end{bmatrix}$$

As discussed, we assume Z_n is small so we can ignore the T_{xz}, T_{yz}, and T_{zz} terms. Then the transfer function relation becomes equivalent to the three linear equations:

$$X = T_{xx} X + T_{xy} Y_n + e_x$$

$$Y = T_{xy} X_n + T_{yy} Y_n + e_y$$

$$Z = T_{xz} X_n + T_{yz} Y_n + e_z$$

So now we can formulate the general form of the transfer function for induced fields:

$$B_t = T_{bx} X_n + T_{by} Y_n + e_b$$

where B_t is the anomalous field component, X_n and Y_n are the normal component, T_{bx} and T_{by} are the horizontal transfer functions, and e_b is the uncorrelated noise in signal.

The vertical field anomalies are a diagnostic indicator of lateral inhomogeneities in conductivity. Furthermore, our assumptions include the expectation that X_a and Y_a are small compared to X_n and Y_n. So we restrict our studies to vertical field anomalies and will work

with:

$$Z = T_{xz} X_n + T_{yz} Y_n + e_z$$

The transfer functions are complex due to the inductive nature of the image currents. The three field components were recorded and transfer functions were calculated by minimizing the signal error term e_t. The transfer functions were calculated using the robust statistical processing scheme of Egbert and Booker (1986). This linear relation between horizontal and vertical components is then used to interpret the array data.

In a sense, this analysis can be related to the case of composing the vertical field from two orthogonal source fields:

$$Z = AX + BY$$

The transfer functions A and B are invariant under rotation. Often we want to measure the fields in geomagnetic coordinates but the source field is arbitrary or unknown. Conventionally, $\hat{x}$ is taken as geographic north, $\hat{y}$ is taken as geographic east with $\hat{z}$ increasing with depth. Any source field can be broken into components for two orthogonal polarizations, thus:

$$Z_E = A'X_E + B'Y_E$$

$$Z_B = A'X_B + B'Y_B$$

A′ is a transfer function, which is related to regional source fields. This gives us two equations in two unknowns, hence we may determine the transfer functions in coordinates for an arbitrary regional field.

$$A' = \frac{Z_E Y_B - Z_E Y_E}{X_E Y_B - X_B Y_E}$$

$$B' = \frac{X_E Z_B - X_B Z_E}{X_E Y_B - X_B Y_E}$$

In the literature these two orthogonal polizations are referred to as E′ and B′ or $E_\perp$ or $E_\parallel$, where these transfer functions can be used to delineate the directions of maximum and minimum correlation between horizontal and vertical field components. In a two-dimensional earth we would expect that if the regional source field, say X_n, was aligned with the local structure, then

$$Z_B = A'X_n$$

and the vertical field would be strongly correlated with the source direction. Correlation coefficients for Z and H greater than 0.8 are rarely observed in the earth because the ionospheric sources are only approximated by a plane wave. So, if the direction of maximum response can be found, then we can determine the strike of geoelectric structure. This direction may correspond to the strike of geologic structure if the local structure is approximately two dimensional, and conductivity contrasts are sharply defined.

The graphic presentation of these transfer functions developed by both Parkinson and Wiese are known as induction vectors. The vertical transfer functions at a given station can be reduced to a real and imaginary induction arrow, v_r and v_i. If a two-dimensional conductivity contrast exists near the station, there will be a local concentration of current close to the boundary, and a part of the vertical field will be correlated with the horizontal field. The direction of the horizontal field for which this correlation is a maximum is perpendicular to the current concentration and defines the direction of the transfer function. Its amplitude is the ratio of the correlated parts of the vertical and horizontal field in this direction. The induction vectors are found from the equation:

$$v = (-ReA, ImA) \, \hat{x} + (-ReB, ImB) \, \hat{y}$$

As a complex quantity, we can find real and imaginary components of the induction vectors:

$$l_r = \left[(ReA')^2 + (ReB')^2 \right]^{\frac{1}{2}}$$

$$l_i = \left[(ImA')^2 + (ImB')^2 \right]^{\frac{1}{2}}$$

Induction arrows also have an azimuth, θ_r or θ_i, associated with each component:

$$\theta_r = \sin^{-1} \left[\frac{(-ReB')}{l_r} \right]$$

$$\theta_i = \sin^{-1} \left[\frac{(-ImB')}{l_i} \right]$$

The azimuth of v_r indicates the direction of maximum gradient in conductivity. For a two dimensional structure, v_r will point towards a more conductive region and is perpendicular to the geoelectric strike. Interpretation of θ_i is inherently difficult due to the nonuniqueness of

the phase. There is no way to assign a consistent sign convention for the v_i because the imaginary arrows reverse direction as the inducing period varies. The recent discussion by Chen and Fung(1985) points out the constraints on using imaginary induction arrows to interpret geoelectric structure. In this experimant, I will rely mainly on using v_r to locate lateral conductivity constrasts within the crust.

CHAPTER 3

Experiment Design

Through the use of transfer functions, the earth can be modeled as a linear filter; when magnetic fields diffuse into the earth they induce currents that flow at a frequency-dependent depth. These currents may in turn be channeled in a DC fashion by lateral variations in the conductivity of earth materials. If the earth were one-dimensional, then the magnetic fields at the surface would have no vertical component; the source current and induced current both produce fields which produce secondary magnetic fields which cancel each other out. However, the earth has two- and three-dimensional electrical structure which leads to magnetic variation anomalies caused by the local induction and channeling of regional currents. Where a lateral inhomogeneity exists, a vertical field component will be measured at the surface. These variations have been related to a number of large scale geologic structures such as continental rifts in Kenya and New Mexico as well as hot spots and subduction zones. (Beamish, 1977; Schmucker, 1970; Kurtz et al, 1986) The aim of this experiment was to search for a conductivity anomaly associated with the southern edge of the subducted Gorda Plate.

3.1 Experiment Background

There are at least four likely processes that could result in higher electrical conductivity at depth south of the plate boundary: (1) the upwelling of hotter asthenospheric material into the void created by viscous drag from the southward motion of the capping lithosphere; (2) the presence of partial melt in the rising asthenosphere; (3) the release of fluids from minerals such as serpentine (which is widely distributed in the Franciscan Formation) as the Coast Range lithosphere heats up above 500° C (Parkhomenko, et al. 1973; Dvorak, 1973); (4) the increased solubility of ions in warmer interstitial fluids. Fluids subducted with the Gorda Plate could also result in enhanced conductivity north of the boundary as has been reported for subduction under Vancouver Island (Kurtz, *et al.*, 1986). Such an effect is less likely in northern California due to the thinner sediment cover of the Gorda Plate (Silver, 1971) in contrast to the Explorer Plate.. The first two mechanisms would be evident immediately south of the plate edge, while the other two will manifest themselves further south as the heat

diffuses up into the lithosphere.

The relation between conductivity and temperature is typically

$$\sigma = \sigma_0 \exp \left[\frac{(-E + P\Delta V)}{KT} \right]$$

where E is the activation energy, ΔV an activation volume expressing temperature dependence, K the Boltzman constant and T the absolute temperature. From the work of Shankland (1985), a conductivity of 0.1 S/m would be predicted with a melt fraction of 0.1 for mantle materials at 1100° and 30 Kb. I would not expect to observe such high melt fractions in the mechanically rigid crust. If such high conductivity material is found in the lithosphere, that is outside of volcanoes, then other processes must be acting to increase the conductivity. One likely candidate is the chemical effect of volatiles such as H_2O, CO_2, and SO_3 that increase conductivity in a dramatically non-linear fashion. For example, an order of magnitude increase in forsterite conductivity results from exposure to an H_2 rather than O_2 atmosphere. (Morin et al, 1977)

A number of factors, including the dewatering effect and elevated temperatures, may cause an abrupt change in conductivity south of the Gorda Plate edge. The maximum heat flow actually occurs 250 km south of Cape Mendocino, equivalent to 5 MY after crossing over the half spreading center. A reasonable first approximation to the expected overall anomaly is therefore the edge of a nearly horizontal conductive tablet which should become progressively deeper to the east and may become shallower to the south.

The regional electrical structure can be approximated as a resistive layer which crops out in the Coast Range and is overlain to the east and west by thin near-surface conductors: the highly conducting ocean and the sediments of the Great Valley. Furthermore, the geologic structure of the Coast Range south of Cape Mendocino also has a north-south trend. The entire structure overlies a good conductor at asthenospheric depths (Schmucker, 1970). An anomalous zone associated with the spreading center could protrude up into the resistive layer and cut across the regional structure.

For a horizontal inducing magnetic field perpendicular to a buried cylindrical conductor, currents flowing in the conductor produce a vertical magnetic field which reverses over the conductor. The same source over the edge of a semi-infinite conducting tablet or sheet results only in a single maximum of the vertical field which is displaced towards the resistive

side of the edge. In either case, if the source is along strike no vertical field is produced. Thus the anomalous vertical fields in the Coast Range due to the ocean and other regional structure are maximum when the inducing magnetic field is approximately east-west. Their anomalous vertical fields should be small and the anomalous field of the buried half spreading center which cuts across the regional structure should stand out best when the source field is north-south. Furthermore, if the measurements are made at a constant distance from the coast, incomplete suppression of the strong coast effect due to a wrong choice of source polarization will enter as a constant bias. For these reasons, our basic experiment involves interpreting the vertical field for north-south source polarization along profiles parallel to the coast.

Table 1. summarizes the anomalous field response due to a two-dimensional edge discontinuity in surface conductivity (from Fischer, 1979). The structure typifies an idealized coastal edge anomaly where the coastline is presumed to run in the $\hat{x}$ direction and the conductivity changes in the $\hat{y}$ direction. Clearly for a magnetic source field, H_o, polarized perpendicular to this coastline ($E_\parallel$ mode) the coastal edge anomaly is maximized. For a source polarization parallel to the coastline, no coastal edge anomaly would be observed. Few continental margins mimic this simple two-dimensional model of a coastal edge. Studies in southern California (Schmucker, 1970) and southeast Australia (Hyndeman and Lilly, 1968) nonetheless were able to discern conductivity anomalies in the midst of three-dimensional geolectric structure by employing an $E_\perp$ interpretation. In southeastern Australia, Everett and Hyndeman removed the coast effect contribution to the transfer functions based on their distance from an ideal (linear) coastline that extended over 600 km perpendicular to the strike of their transect. In my study area both the Mendocino Fracture Zone (MFZ) and the irregular coastline complicates the construction of such an "ideal coastline". The dog leg bend in the coastline cuts off any ideal coastline only 100 km north of the array's center. Offshore, the Mendocino Fracture Zone (MFZ) introduces a 1-1.5 km decrease in bathymetry north of the Cape Mendocino promontory.

3.2 The Field Study

In the summer of 1986, Univerity of Washington researchers deployed an array of three-component magnetometers at sites south and east of Cape Mendocino (Figure 3.2.1). Nine instruments were used in three separate deployments. Each deployment involved at least two sites which overlapped with the previous deployment. The complete array of 18

sites consisted of 3 north-south transects, that extend south from 40.5° to 39° latitude. At least ten days of data were digitally recorded at each site and anomalous vertical fields were computed using a robust estimation technique (Egbert and Booker, 1986) that discriminates against external anomalous vertical fields and other coherent and incoherent noise sources.

Table 1. Magnetic Field Response for a Coastal Edge Anomaly

|	$E_{\parallel}$	$E_{\perp}$
Horizontal magnetic field	H_x can vary appreciably close to shore especially on conductive side of edge.	H_y is uniform.
Induction range of coast effect, L_0	The induced currents parallel to shore have an effect over wide range on land and sea . $L_0 = 0–2\delta_0$	Edge effect apparent only over short range. $L_0 \ll \delta_0$
Correlation	$Z = H_z/H_y$ is well correlated.	$Z = H_z/H_x$ is very weakly correlated
Induced fields	E_x, H_y, H_z	E_x, E_z, H_x
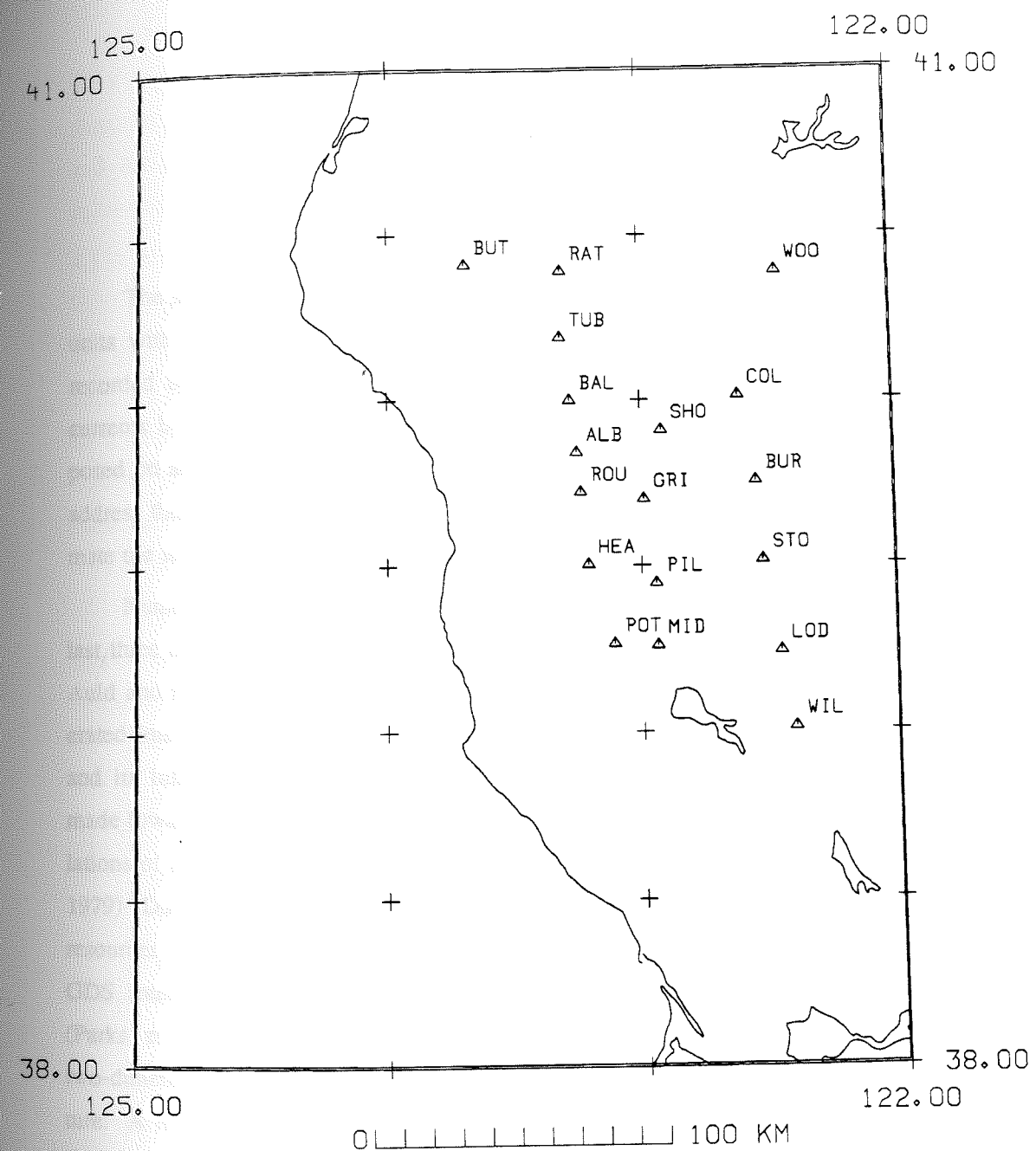
Figure 3.2.1 Station location map showing magnetometer sites and array geometry for the experiment. The dashed line indicates the trajectory of the plate edge inferred from gravity data. This experiment will also attempt to locate this boundary by interpreting anomalous vertical fields recorded along N-S transects of the array.

CHAPTER 4

MODEL DESIGN

The surface geology of the Northern Coast Ranges contains a numerber of conductive units with a variety of regional strikes. This complexity could affect the magnetic fields recorded by the array due to the coastal edge anomaly and channeling of regional telluric currents by local inhomogenieties in conductivity. These local variations would be superimposed on any conductivity anomaly arising from deeper asthenospheric structure. In order to address these issues, interpretation of this experiment will include numerical models that estimate the importance of three-dimensional surface conductors on the magnetometer array.

Numerous induction experiments have been performed on continental margins in the last three decades. (Everett and Hyndeman, 1967; Schmucker, 1970; Bailey et al,1974; Law, Auld and Booker, 1980; Hensel, 1982; Egbert, 1987) Interpretation of these works has generated interest in understanding the complicated geoelectric structure of continental margins and its influence on resolution of tectonic features found there. Much progress has been made towards a theoretical understanding of the "coast effect" since the first analytical calculations of two-dimensional thinsheet conductors in the mid-1970's. (cf. the review by Fisher, 1979) Due to the increased availability of high-speed computers with large memory resources, the three dimensional aspects of surface features in general are often included in GDS interpretations. The necessity of this scrutiny is highlighted by two recent works (Parks, et al, 1983) and (Wannamaker, et al, 1984) that both discuss the pitfalls of applying two-dimensional interpretations in areas that may be dominated by three dimensional structure. A related problem in GDS studies is current channelling or the "gathering" of regional currents by surface conductors (Jones, 1983). Clearly, my attempt to image deep crustal structure even with long period data must address the effects of the irregular coastline and truncated Sacramento Valley. In light of the known surface conductors in the Cape Mendocino region, I have used a three-dimensional thinsheet modeling program in attempt to estimate their effects on the observed fields.

This chapter discusses the design and implementation of the numerical model on a Cray-XMP computer at the San Diego Supercomputer Center. Section 4.1 identifies the dominant geoelectric features of the surface geology in northern California. The assumptions and limitations of the thinsheet approximation are outlined in Section 4.2. Finally, the numerical model chosen to represent the California Coast Ranges is presented in Section 4.3.

4.1 A Model of Conductivity Structure in the Northern Coast Ranges

Induction experiments are quite often the pioneering study of geoelectric properties in any given field area. Before the array is deployed, little information is available on the conductivity of the surface geology or crustal features in the region. The same problem exists in an attempt to model a proposed field area for an experiment. In the case of the northern California Coast Ranges, more information is available than in other locales. This section uses a combination of well log data, geothermal exploration surveys and two unpublished MT surveys to create a model of conductivity structure in the array study area.

From proprietary data and the work of Stanley (1973) near the Clear Lake geothermal area some DC resistivity soundings are available to constrain the electrical structure of the following major geologic units:

(1) The upper crust of the continental margin is moderately resistive (.002-.001 S/m) down to a depth of 30 km. This unit includes the granitic rocks of the Sierra Nevada and the Cascades.

(2) The lower crust, from 30 to 80 km, is also resistive, with a value of .002 S/m.

(3) Significant alluvium and gravel fills the Sacramento basin of the California Great Valley. The depth of valley fill varies from 3 to 4 km on average on the east side of the Corning Fault, and may be as deep as 6 km on the northwest side, as indicated by logs of a deep well near the Vilche Ranch (Harwood, 1987). Measurements by Stanley and well log data suggest that these sediments can be quite conductive, with σ varying from .5 to .2 S/m.

(4) Imbricated slices of Great Valley Sequence appear along faults throughout the Coast Ranges. These coarse clastic rocks of Jurassic Cretaceous age are also very conductive and will be grouped with alluvium of the Great Valley with conductivities .2 to .5 S/m.

(5) The continental margin along the coast is covered by Coast Range rocks, a subduction melange ranging from 5 to 10 km in thickness which overlies crystalline basement. The sequence contains moderately metamorphosed sandstone conglomerates, basalt, amphibolite and serpentinite. Consequently, Stanley observed significant variation in resistivities. His work suggests σ varies from .2 to .04 S/m in clastic members to values less than .005 in volcanics and serpentinites. In the fall of 1988, a Univ. of Oregon research team occupied 10 MT sites in the nortwestern section of the array. Their preliminary results indicate a relatively high conductivity of .03 S for the Coast Range

rocks. (Waff, 1988; private comm.)

4.2 The Thinsheet Approximation to the Induction Equations

In this section, I discuss a computer program that calculates the magnetic field response that three-dimensional conductivity structures such as surface geology might produce. The numerical model consists of a thinsheet which overlies a one-dimensional layered halfspace. (Figure 4.2.1) The thinsheet contains the lateral variations in surface conductivity for the study area. An integral equation technique solves for induced fields in the basal halfspace. The thinsheet approximation is then used to determine field values at the surface. The thinsheet approximation for solutions to the induction equation was first developed by Price (1949). The theory and numerical solution techniques of Weaver and Dawson (1978) were used in this case.

Analytic solution of the induction equation is made in each of the three regions: $z < 0$, $0 < z < d$ and $z > d$. These solutions are coupled across interfaces at $z = 0$ and $z = d$ by use of the boundary condition on tangential E. The interface $z = d$ is assumed to have zero conductance. At $z = 0$, the thinsheet approximation is employed to represent the conductivity of the surface layer by a grid of conductance values.

In order to create a thinsheet model of the Coast Ranges, the top 4 km of the study area was represented by a grid of integrated conductivities. The region was mapped onto a 30x30 grid using a grid spacing of 40 km. For solution accuracy the grid spacing should be no greater than $\delta_0/3$ or $\delta_0/4$, where δ_0 is the skin depth in the first layer underlying the thinsheet. Often, model design would dictate much smaller grid spacing, on the scale desired for adequate resolution of geologic features. In this study, model responses were calculated at a period of 900s, a value that allows a sufficiently fine grid spacing to resolve major geologic structures while still allowing at least one skin depth of buffer at the sides of the model.

Analytic solution of the Helmholtz equation requires the imposition of boundary conditions at the surfaces of the volume. For $z < 0$, the behavior of the total field is determined by the source field, which is calculated from a sheet current at altitude. Dissipation of wave energy with depth required the total fields to vanish as $z => \infty$. Boundary conditions are imposed on the sides of the model area by solution of a well defined two-dimensional problem as $|x| => \infty$ or $|y| => \infty$ respectively. The restrictions:

$$\lim_{|x| \Rightarrow \infty} \frac{\partial(E, B, \tau)}{\partial x} = 0 \qquad \lim_{|y| \Rightarrow \infty} \frac{\partial(E, B, \tau)}{\partial y} = 0$$

specify the gradients of both the fields and the conductances on the model edges.

Thus, an accurate solution requires a vanishing gradient of field values on the sides of the grid. In effect, this allows no current to channel in the invariant direction at the edges. If any conductance boundaries are located too closely to the grid edges the solution accuracy will suffer. This consideration motivates the modeling design rule of locating the grid edges at least two skin depths away from any conductance boundary. If violated, the field values at the edges will not vanish and may introduce a DC offset to the profile of field values. Weaver and Dawson recommend that the grid be at least several (~5) skin depths on a side to allow spatial separation of the unrealistic current distribution at the edges.

This last step of the solution uses the boundary condition for tangential fields at an interface first employed by Price (1949). Obviously then some criteria are needed to describe whether the surface layer is "thin" enough to approximate as an interface. Weaver (1982) developed two conditions on the maximum thickness of the surface layer by requiring that the attenuation factor of electric field in the thinsheet be less than 0.10. These conditions are:

(1) $h \ll \delta$ where h is the thickness of the surface layer and δ is skin depth in underlying layer.

(2) $h^2 \ll n^2$ where n is the skin depth in the surface layer.

The values for these criteria are included in Table 2. The numerical model is adequate for longer periods but the attenuation is significant at periods less than 900 s. The effect of the attenuation will be to decrease the electric fields diffused through the surface layer as compared to the magnitudes calculated by the model. Consequently, during interpretation of the models, the reader must bear in mind that field magnitudes may be somewhat overestimated as the induction parameter, $\frac{h^2}{n^2}$ is marginally small enough at T=900 s.

4.3 The Numerical Model

The numerical model chosen to represent the California Coast Ranges are shown in Figure 4.3.1. The conductances are given in Table 3. The major geologic units studied by Stanley have been included along with the bathymetry of the continental margin. Note that a conductivity value has been assigned to each of the $N^2 = 900$ grid cells in the mesh. The vertical conductivity structure is shown in Figure 4.3.2. The surface thin sheet overlies a

two-layered half space. Certainly the deep electrical boundary of the continental margin is more complicated than this simple structure. Nonetheless, this model will estimate a minimum bound for the GDS response from the surface geology. Any differences between this model of surface conductors and the array data may be reliably attributed to structure deeper than 4 km.
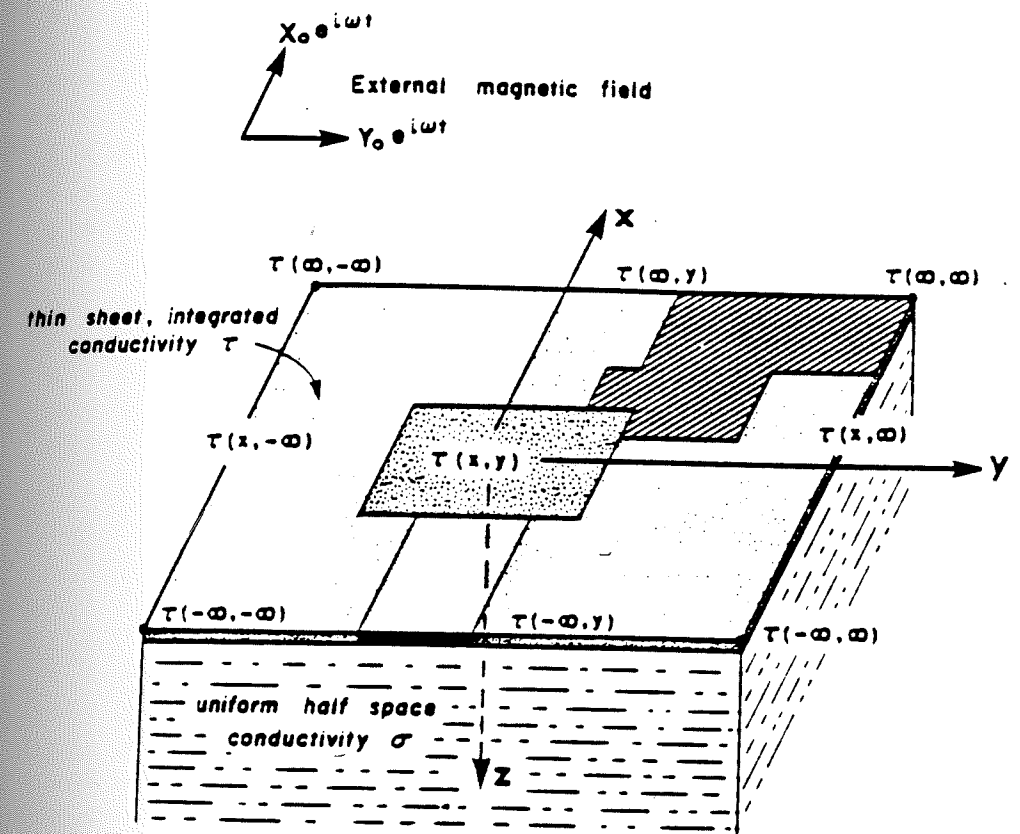
Figure 4.2.1 Schematic model of the generalized thinsheet problem. Thinsheet extends from z=0 to z=d. A one-dimensional layered halfspace extends from z=d to infinity.

Table 2. Approximation Criteria for the Thinsheet Model

Model	$h/\delta_0 \ll 1$	$(h/n)^2 \ll 1$
T300	.021	.666
T900	.012	.227
T2700	.007	.070
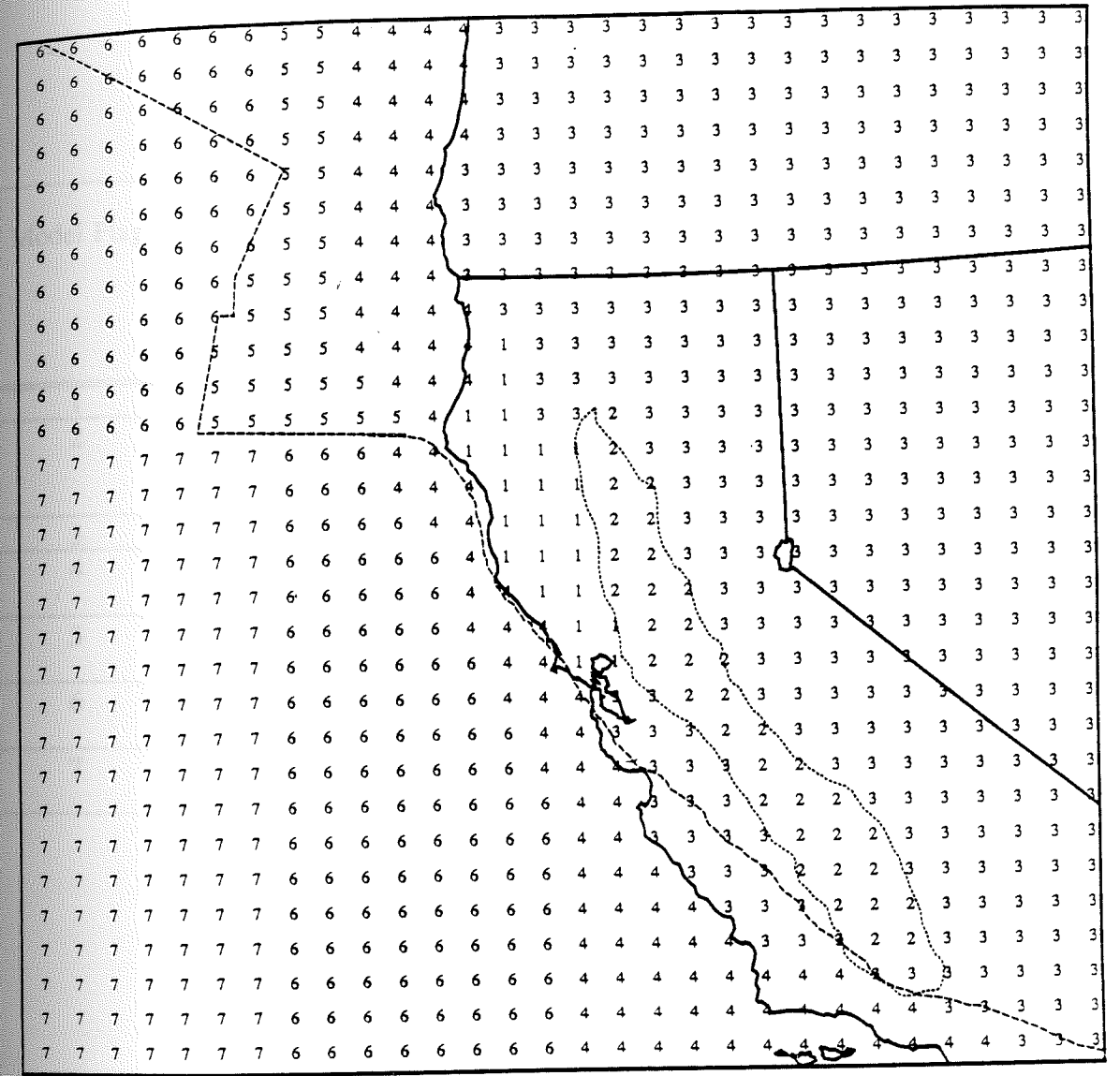
Figure 4.3.1 The map displays the numerical grid used to represent the major surface geoelectric units of the Northern Coast Ranges, California. The dashed line shows the boundary of the Juan de Fuca Plate offshore and merges with the trace of the modern San Andreas Fault. The dotted line marks the boundary of the units mapped as Great Valley Sequence and Quaternary alluvium of the Central Valley.

Table 3. Conductivity Structure of the Thin Sheet Model

Model Flag	Map Unit	Conductivity (S/m) σ_n	Dimensionless Conductance $\lambda = \dfrac{\sigma_n z_o}{\sigma_o \delta_o}$
1	Coast Range Metasediments	.033	.199
2	Great Valley Sequence and Sacramento Valley Alluvium	.200	1.19
3	Continental Crust	.002	.0119
4	Shallow shelf h=500m	3.2	2.35
5	bathymetry h=2000 m	3.2	9.56
6	bathymetry h=3000 m	3.2	14.3
7	bathymetry h=4000 m	3.2	19.10

Figure 4.3.2   Vertical Conductivity Structure of the Thin Sheet Model

$z = 0$ km _____

$\sigma = \sigma_n$

$z_o = 4$ km _____

$\sigma_o = .002$ S/m

$z_h = 150$ km _____

$\sigma_h = .1$ S/m

CHAPTER 5

DISCUSSION

In this chapter, results from the magnetometer array and from the three-dimensional model are presented. Two different presentations of the array data are made in Sections 5.1 and 5.2. First, induction arrows are displayed and discussed in terms of the frequency response of their magnitude and azimuths. Next, hypothetical event analyses are presented for the stations that demonstrate the difficulties of selecting the appropriate source polarization for the $E_\perp$ interpretation. Finally, in Section 5.3, results from the thinsheet modelling program are used to demonstrate the effects of surface conductors on the measured fields. A number of important features of the induction array are duplicated by the model results.

5.1 Induction Vectors for the Array

Real and imaginary induction vectors for the array are plotted for four period bands in Fig 5.1.1. In a two dimensional structure, both the real and imaginary arrow would point perpendicular to geologic strike. The degree to which these two arrows depart from coplanarity is an indication of three dimensional structure. Wiese's convention is used so that the real induction arrow (v_r) will always point toward the direction of increasing conductivity. Each pair of arrows originates at a magnetometer site; the reader may refer to Figure 3.2.1 for station names. The real and imaginary arrows both radiate out from the station site and are shown with solid and dashed lines respectively. The blocks that serve as arrowheads show the error in azimuth and magnitude, where the bars are separated by 2 standard deviations. In general, the errors are quite small, less than 5 percent.

For a period of 60 sec., both magnitudes and azimuths of the induction arrows vary widely. Also, in the northern half of the array as well as along the eastern profile, the azimuths of v_r and v_i are poorly correlated. Evidently, the complicated surface geology controls the variation of magnetic fields in this period band. Some features of note are:

i.   Vertical field magnitudes are greatest on the east side of the array near the edge of the Great Valley. v_r has both a large eastward component as well as a smaller southern component than in the western profile.

ii. Stations POT and MID are clearly affected by the wedge of tectonically emplaced GVS. Magnitudes are reduced at POT which lies within the GVS wedge. Both the azimuth and magnitude of induction vectors for MID are influenced by this same wedge of more conductive material.

iii. The directions of $\mathbf{v}_r$ at stations RAT and BUT is more northerly than for the rest of the western lines. In this northern part of the western profile, the magnitudes of field values are enhanced relative to values to the south. This deviation could be an effect from the irregular coastline north of Cape Mendocino, though the stations are located in the center of the Cape Mendocino promontory. Alternatively, these stations may be distorted by a the thick cover of Tertiary sediments near Hayfork, 20 km to the north.

iv. The azimuths of the $\mathbf{v}_r$ rotates from southwest to southeast from the western to the eastern profiles.

v.   The direction of $\mathbf{v}_r$ at station WOO is clearly south. This station is only 20 km south of the northern terminus of the Sacramento Valley and may be strongly influenced by the three-dimensional nature of this terminus.

For a period band around 300 s the magnitudes of the transfer functions becomes more uniform in general throughout the array. $\mathbf{v}_r$ and $\mathbf{v}_i$ are not coplanar though along the western profile a general trend towards the two components lining up is noticeable. This would be expected as the skin depth of the sounding extends into the more homogeneous resistive basement underlying the Coast Range. Along the eastern profile, no such trend is observed; the $\mathbf{v}_r$ rotate south with little or no eastward component.

Around a period of 900 s, magnitudes of $\mathbf{v}_r$ continue to increase. The transfer functions are more uniform across the array and reflect the strong magnetic fields produced by the coastal edge anomaly. Also, $\mathbf{v}_r$ and $\mathbf{v}_i$ are nearly parallel on the western side of the array. The average azimuth of $\mathbf{v}_r$ in the central western portion of the array suggests choosing $-15°$ relative to geographic north for the source polarization in the $E_\perp$ mode. This is not coincident with the local coastline, which trends more westerly in the region south of the Cape Mendocino promontory and trends northerly further to the north near the Oregon border, but may reflect an overall average coastline. Thus, induction arrows may be rotated by some geoelectric feature other than the local coastline, a situation which complicates a simple two-dimensional analysis. The azimuths of the two components are still divergent along the eastern transect which now has no eastward $\mathbf{v}_r$.

The magnitudes and azimuths of the westmost vectors calculated for the 2700 s period band become quite uniform on the two western traverses. Magnitudes of $\mathbf{v}_r$ continue to increase while the azimuths are generally oriented perpendicular to the coastline. The

magnitudes of v_i have decreased and a general coplanarity between real and imaginary components is evident. Three-dimensional effects are still apparent along the eastern traverse.

For periods near 3500 s, imaginary components are quite small across the array, except for the northwest corner. Magnitudes of the real component have increased presumably reflecting the large electric current induced on the seaward side of the continental edge. The magnitudes of the real component are anomalously smaller in the northwestern corner, considering the proximity of the stations to the shore. The small imaginary component suggests that currents are no longer governed by induction in local structures but are instead a conductive feature.

Qualitative conclusions regarding the importance of near-surface and buried conductors are derived from the frequency dependent behavior of the long-period induction arrows. The dominant feature that controls the size and orientation of the induction arrows is the coastal edge. The Coast Range Thrust, which emplaced a wedge of GVS over a Franciscan ophiolite complex, and the adjacent Sacramento Valley also creates an surficial edge anomaly. The azimuths of the v_r are plotted in Figure 5.1.2. The orientation of the real component changes with frequency, demonstrating that three-dimensional effects must be included in the structural analysis. Thus a single source polarization should not be used for a hypothetical event analysis at all periods. If this were done, then the effects of three-dimensional structure would be erroneously attributed to conductivity changes with depth.

Perhaps the most interesting aspect of the array data is that the imaginary component is fairly homogeneous in size and sign for the periods 300 s < T > 3000 s. From the diffusion wavelengths shown in Table 4, I would expect more variation if the phase of the magnetic fields at the surface were derived solely from a layered model of metasediments upon resistive basement. The magnitudes of v_i are generally large throughout a broad period band. One explanation for the homogeneous v_i is that the array response is dominated by a channeled current that acquired its phase from induction at another location, probably offshore. This is puzzling in context of the DC response predicted by Beamish (1987) for conductive line currents at $T > T_c$, i.e. for two dimensional structures past the inductive limit. Interpretation of imaginary induction vectors is inherently difficult but this behavior is consistent with the leakage of current from the coastal edge into the conductive metasediments of the Coast Ranges. Similar effects from the channeling of currents in sediment wedges along the St.

Lawrence River were discussed by Bailey, et. al. (1974) Alternatively, the adjustment distance of the induced currents could be lengthened by the high conductivity values of the Coast Range metasediments and Sacramento Valley. This scenario would have the currents flowing at shallower depths in the Coast Ranges than its conductivity structure alone would predict; in effect, the vertical adjustment of currents to continental structure may not occur until east of the Sacramento Valley.

5.2 Hypothetical Event Analysis

Interpretation of GDS data is greatly simplified if the earth structure resembles a two dimensional profile. Hypothetical event analysis (HEA) presents induction data in a manner that allows easy comparison with two-dimensional models. A HEA is the calculation of the anomalous magnetic fields that would have resulted from a unit amplitude magnetic field variation of a selected polarization in the horizontal field. In this paper, source polarization, θ_s is reported as the azimuth in degrees relative to geographic north. This method of data presentation was first suggested by Bailey et. al (1975) and has been used frequently in rift and continental margin settings by Beamish (1977) and Egbert (1988). While there are hazards in employing a two-dimensional interpretation in an area with numerous lateral inhomogeneities, depending on the length scales and conductivity of local bodies, an $E_\perp$ interpretation may still suffice. My objective in the first part of the data analysis is to determine the source polarization for which anomalous fields from the buried plate edge are large compared to the anomalous fields generated by surface conductors.

This section uses HEA's for the array to demonstrate the variation with period of the source azimuth that yields the maximum response in the vertical field, Z. Table 5 lists the transfer functions for a source polarization due E and due N respectively. All HEA were calculated from these values with both horizontal and vertical fields taken from the individual station. The use of single-station HEA differs from the more common use of the horizontal magnetic field at one station as a remote reference for all of the array. My approach is justified in this case because both the transfer functions and the anomalous horizontal fields are small. This implies that horizontal fields are fairly uniform across the array.

A degree of geologic interpretation is inherent in the choice of source polarization for an HEA. The experiment design depended upon choosing a source polarization θ_s perpendicular to the dominant geoelectric strike of surface features near Cape Mendocino. As I expect

the coastal edge effect to provide the dominant anomalous fields, the first task required in HEA of the array is the selection of a θ_s that minimizes the coastal edge anomaly. I expect a θ_s that is perpendicular to the given θ_r at a certain period would minimize the large anomalous fields induced at the coastal edge. In Figure 5.1.2 the azimuths of v_r at a range of periods is displayed. These show that it is necessary to select a different θ_s in order to obtain the minimum response for each period band. Simplistically, I have taken an average value of θ_r from the western and middle profiles to estimate the correct θ_s for each period band. The eastern profile was ignored due to the likelihood of strong influence from the valley fill. Stations POT and MID were also neglected due to the wedges of Great Valley Sequence rocks under these stations.

Figures 5.2.1 and 5.2.2 plot the real and imaginary components of Z for a mixture of source polarizations selected to maximize the $E_{\parallel}$ response for each period band. Then the HEA was repeated with a θ_s rotated $-90°$ from the source polarization for the $E_{\parallel}$ mode. The resulting anomalous fields for the $E_{\perp}$ mode are plotted in Figure 5.2.3 and 5.2.4. In the next chapter, plots of Re(Z) and Im(Z) from this HEA will be compared with fields from a two-dimensional model of a step in the aesthenosphere.

It is clear that the "average coastline" that contributes to the coastal edge anomaly changes with period. Table 6. lists the value of θ_s chosen for each period band. A study of Z values in Figure 5.2.1 and 5.2.3 shows that the magnitude of Z is about an order of magnitude greater for the θ_s chosen parallel to the average coastline rather than perpendicular to it. Thus, the effect of selecting an inaccurate θ_s would be to bias any anomalous fields due to north-south gradients in conductivity such as a buried plate edge might produce. If the structure is approximately two-dimensional, then the wrong source polarization would add a simple linear gradient. However, the distortion in Z could be much more complicated if the surface features are three-dimensional.

5.3 Results from the Numerical Model

In the last two sections, I demonstrated that the choice of a source polarization for interpretation of the array is complicated by three-dimensional effects. Examination of the induction arrow plots revealed that two clear imprints of three-dimensional structure were visible: 1) the variation of optimal source polarization with period, and 2) the divergence in azimuths between the real and imaginary induction arrows. With the numerous surface

conductors discussed in the experiment design, such complications are not unexpected. Therefore, the contribution of surface conductors must be bounded before anomalous fields can be attributed to deeper sources. In this section I propose to estimate the magnitude of anomalous fields that arise from the surface geology.

The thinsheet modeling routines developed by Green and Weaver (1978) and Dawson and Weaver (1979) were used to calculate the vertical magnetic fields contributed by conductors in the upper four kilometers of the study area. With this program, I calculated the electromagnetic field responses for the thinsheet model shown in figure 5.3.1 for the surface geology of the North Coast Ranges. All model calculations were made for a period of 900s. The details of the model were outlined in Section 4.3. except that all of the deep bathymetry (h = 4000) was replaced with intermediate depth ocean (h = 3000m) in order to keep lateral gradients in σ at least one skin depth removed from the edges of the model. The induction arrows calculated solely from surface structures are shown in Figures 5.3.2(a) and 5.3.2(b). The model results reproduce several key features of the array data shown in Figure 5.1.1. This is shown in Figure 5.3.2(c) where induction arrows from the model and the data are plotted at the same scale. There is compelling evidence that the vertical field anomalies observed in S to N profiles of the array are derived from the three-dimensional nature of the coastline and the northern terminus of the Sacramento Valley.

The calculated induction arrows in the model area corresponding to the array have four prominent features: 1) v_r are strongly rotated to the south with values ranging from 40° to 90° S of W; 2) magnitudes of v_i are large; 3) the v_r and v_i are not coplanar; 4) the southward component of v_r has a maximum between Clear Lake and the northern terminus of the valley. These are all features which would also be expected to result from a deep geoelectric boundary with a strike approximately E-W across the lines of the array. Clearly, the model results demonstrate that delineating subsurface structure will be difficult due to the anomalous fields generated by the mapped surface geology and bathymetry.

In order to see more clearly the detailed effect of the surface conductors, W - E and S - N transects across the model are presented for two different source polarizations. In all of the traverse plots presented in this section the origin corresponds to 43° lat. and 123° lon. in the study area. This location is marked with the center tic mark in the induction arrow plots and corresponds to the zero location for the traverse plots.

First, I examine the lateral variations in Z across a S-N (positive distance is to the north) transect of the model at column MM=15 which corresponds to the western profile of the array. A similar transect of the array was interpreted to show evidence of a conductivity anomaly corresponding to the southern edge of the Gorda Plate in a preliminary presentation of array results. (Helferty et al, 1986) The experiment design called for interpretation of variations along just such a transect to search for deeper structure related to a buried plate edge. Figure 5.3.3 shows the variations in Z calculated from the thinsheet model for a source polarization of 0°. The limits of the study area are indicated by tic marks on the y=0 axis. The largest anomaly, with a peak value of .3, is centered over x=-160 km, on the resistive side of the coastal edge. The flanks of this peak extend north to the southern end of the array. Values of Z for the same transect are shown in Figure 5.3.4 with a source polarization of 15°. The peak is reduced to a maximum of .2 but its flank continues to influence the study area.

Next, I examine the lateral variations in Z across a W - E profile through the center of the model for row LL=16. A source polarization of 0° was used. Figure 5.3.5 shows a large anomaly associated with the continental slope falling off to a sloping shoulder with a values near .15 in the study area bounded by the ticmarks. The real and imaginary components are also shown in Figure 5.3.5. Real(Z) is much larger than Imag(Z) except in the vicinity of the continental slope break and the western boundary of the Sacramento Valley. When the source polarization is changed to 15°, the optimal value indicated in the HEA's for this period, the shape of the anomaly changes in the study area. Figure 5.3.6 shows that a decreased amplitude for the peak associated with the continental slope and a isolated secondary peak associated with the western valley edge.

The results of this model suggest that the coastal edge anomaly can influence the study area unless the appropriate source polarization can be used to mitigate its effect. But the trend of the Sacramento Valley is largely north-south in contrast to the strike of the continental slope. The highly conductive valley fill will also contribute significant anomalous fields unless a source polarization along strike is chosen. Model A demonstrates that these two strong surface conductors may preclude a successful $E_\perp$ interpretation for the array data.

Why does a rigorous interpretation hinge on detailed understanding of the surface conducting bodies? Table 3 lists the valley sediments and the deep water as significant conductors, both of which possess three dimensional nature. If one of these features dominates the

vertical field response then a source polarization along its strike would yield the minimum masking of anomalous fields from a deeper source. However, if two or more surface features, of differing strikes contribute a significant amount of vertical field, then the interpretation scheme planned in the experiment design would be misleading. For example, for a source polarization parallel to the Sacramento Valley, the vertical fields along a northerly profile may increase solely due to the greater influence of the northwesterly coastline. The rest of this section will discuss two more models that demonstrate the individual effects of these features on the vertical fields.

The next model demonstrates the effects of the irregular coastline on anomalous fields onland. The conductivity grid shown in Figure 5.3.7 has a constant value for all grid points falling on land. The bathymetry is the same as model A. Induction arrows for model B are displayed in Figure 5.3.8(a) and (b). Once again the azimuths of v_r are rotated to the southwest. This rotation persists for 300 km south of Cape Mendocino. Figure 5.3.9 shows the vertical field anomaly for row LL=16, which corresponds to the center of the magnetometer array. A large broad anomaly begins at the continental slope break and extends inland for 200 km. For the S-N traverse, shown in figure 5.3.10, a double peaked anomaly reflects the transition from intermediate depth ocean to continental shelf as well as the coastline crossing. The northern anomaly begins at x = -200 km, where the traverse crosses onto land. Through most of the array area in the model, Real(Z) values are decreasing linearly with increasing distance from the continental shelf. For other source polarizations this transition is not linear; instead small undulations are superimposed on a similar trend.

This model predicts a large magnitude v_r with an azimuth rotated by changing bathymetry at the continental slope. The magnitude of v_r is large and decreases with increasing distance from the coastal edge. Most importantly, the southern sites of the study area are clearly affected by the changing orientation of the coastline from Point Cabrillo to Point Reyes. In the area 140 to 200 km south of Cape Mendocino, two components are separated by 20–40°. In the vicinity of Cape Mendocino the v_r and v_i are nearly coplanar. Apparently, the "dog leg" bend in the coastline commencing at Point Cabrillo introduces significant three-dimensional effects. This skewness demonstrates that no single source polarization can be used to construct an $E_\perp$ interpretation at T = 900 s.

In this next model I examine the effect of the truncated northern end of an an idealized

alluvial basin. Model C consists of the sea to Sierran transition as shown in Figure 5.3.11. However, a three-dimensional complication is included by truncating the Sacramento Valley at LL=15. Induction arrows for Model C are shown in Figure 5.3.12(a) and (b); The v_r on the northwest edge of the valley terminus shows significant southern rotation as well as decreased magnitudes when compared to the more uniform region to the north. The rotation increases from southwesterly at 120 km north of the terminus to due south along the western edge of the valley. The rotation drops off quickly to the south, vanishing within 100 km of the terminus. The truncation of the valley affects the imaginary component of the anomalous fields as well. Small imaginary vectors occur in the model area adjacent to the valley boundary. The traverse plots in Figures 5.3.13 and 5.3.14 plot the variations in vertical fields for this structure. Along column MM=15 the magnitude of v_i is much smaller in the south than north of the terminus. Apparently, the presence of the valley fill prevents the magnetic fields in the south from diffusing as deeply as the fields penetrate to the north. A comparison of Figure 5.3.2(b) and 5.3.12(b) reveals the decrease in length of v_i due to the presence of the valley. Schmucker (1970) discussed this effect for the San Joaquin Valley. Essentially, the conductive valley fill increases the adjustment length of induced currents gathered from the coastal edge. In summary, this model isolates two important effects of the terminus of the Sacramento Valley: 1) a rotation of the azimuth of v_r occurs within 80 km of the northern end and, 2) decreased magnitudes for v_i in the region between the valley and coastal edge.

These three models have identified the major features of the surface geology in the northern Coast Ranges that contribute anomalous magnetic fields to the magnetometer array. However, the limitations of the thinsheet modeling technique must be considered in evaluating the accuracy of these predicted anomalous fields. The most important limitation of this method is the one-dimensional restriction on the subspace beneath the thinsheet. The continental margin of California probably has a significant discontinuity in depth of the lithosphere near the continental slope break, yet such a feature cannot be included in my models. A second source of inacurracy lies in the layered structure assumed for the subspace. In order to avoid overparameterizing the models I chose a simple two layer structure, with a strong basal conductor of 10 Siemens at a depth of 150 km. Weaver demonstrated that the magnitude but not the relative amplitudes of the fields calculated at the surface is dependent upon this depth (Weaver, 1979). The imaginary component of the fields is influenced by both conductivity boundaries and vertical conductivity structure so that conclusions about the v_i predicted by the model are more questionable than those for the v_r.
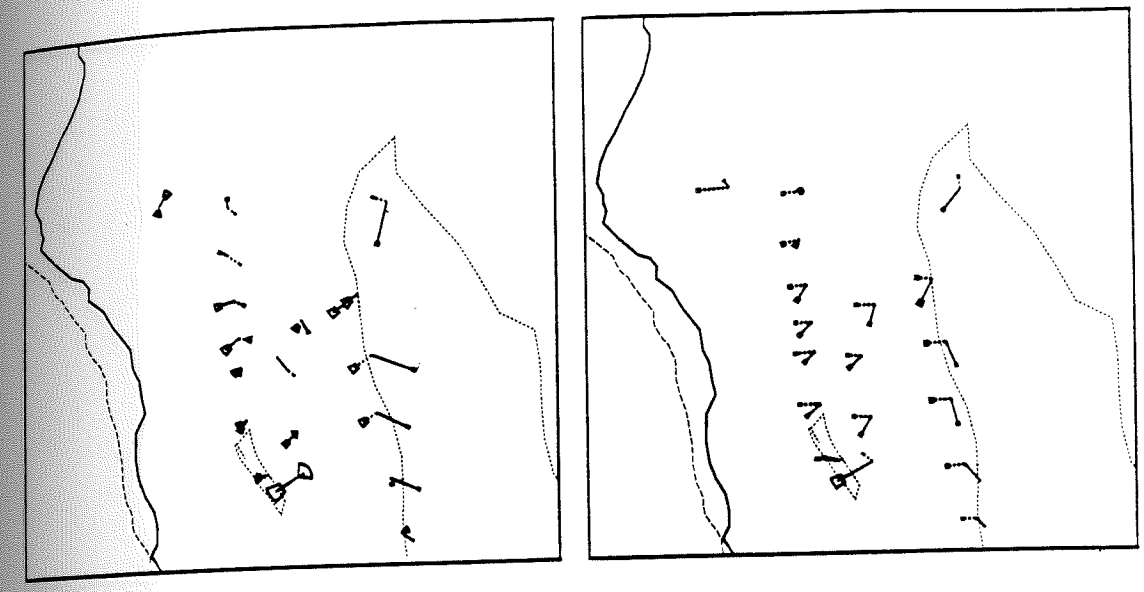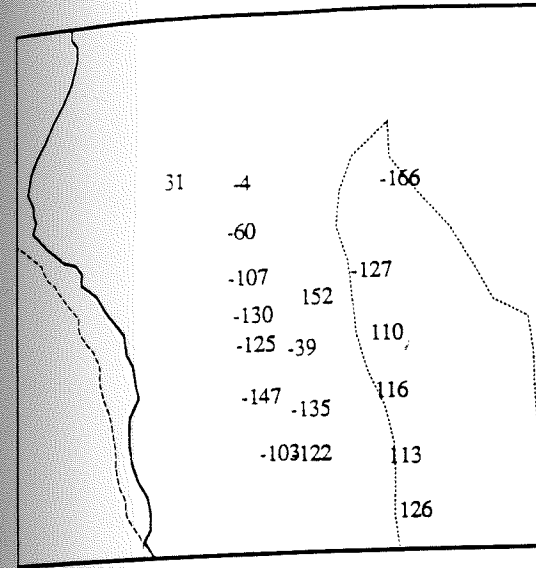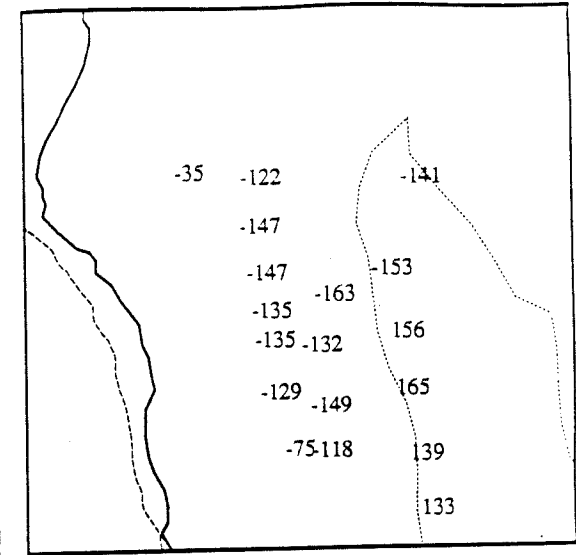
(a) T = 60 s

(b) T = 300 s
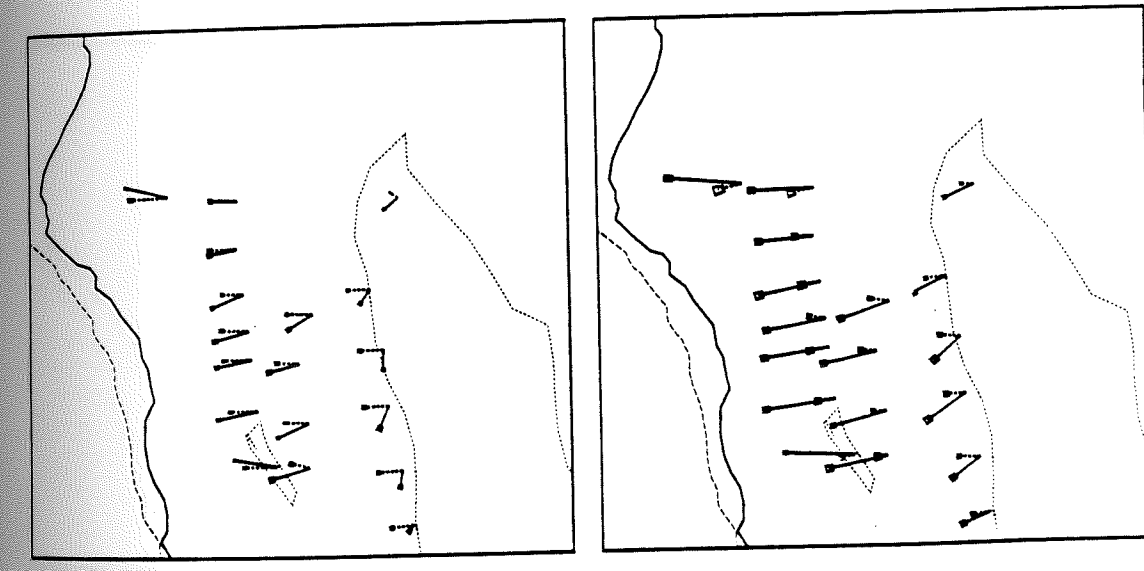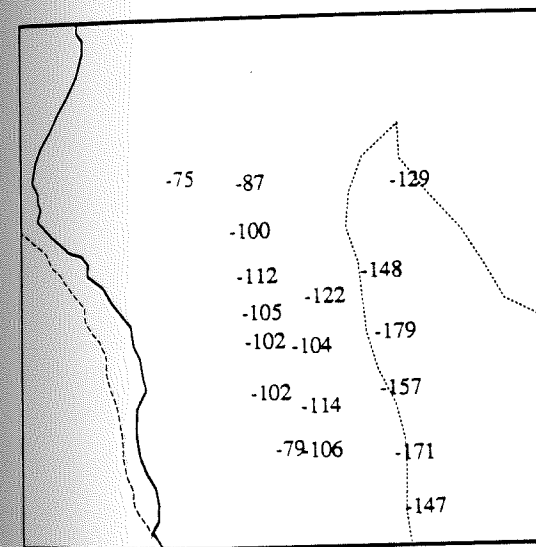
(c) T = 900 s

(d) T = 2700 s

Figure 5.1.1 Real and imaginary induction arrows for the magnetometer array at 4 period bands. The blocks on the end of each arrow show the error in azimuth and magnitude, where the bars are separated by 2 standard deviations.
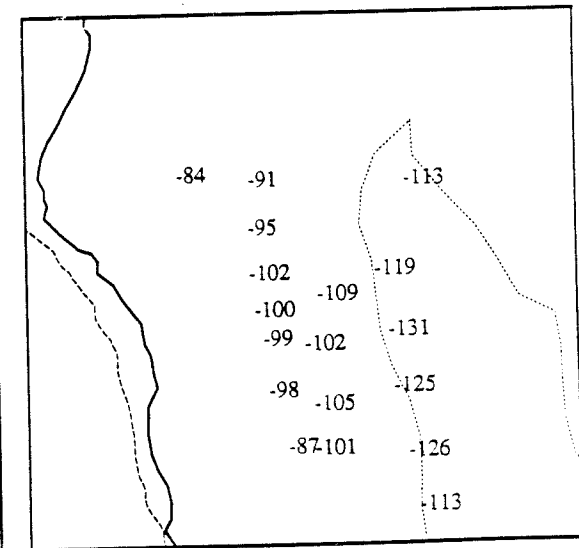
(a) T = 60 s

(b) T = 300 s

(c) T = 900 s

(d) T = 2700 s

Figure 5.1.2 Azimuths of the real induction arrow are presented for the four period bands.
θ_r is measured in degrees clockwise from geographic north.

Table 4. Induction Parameters for the Thin Sheet Model

$$\delta = \sqrt{\frac{\sigma\mu_0\omega}{2}} \approx 1/2\sqrt{\rho T}$$

$$\lambda = 2\pi\delta$$

$$\sigma_1 = .1 \text{ S/m and } \sigma_o = .002 \text{ S/m}$$

Period	δ_1 (km)	δ_o (km)	λ_1 (km)	λ_o (km)
60	21	90	60	540
300	50	190	150	1140
900	80	335	480	2880
2700	140	580	840	5120

Table 5. Transfer Functions for the Magnetometer Array

Z_r^E			Z_i^E			2σ		
2700 s								
447	375	180	-140	-136	-75	27	19	8
	332			-113			18	
376	293	194		-115 -114	-124	21	15	9
	365			-102			16	
397	324	160	-120	-95	-124	18	16	15
423	321	234	-109	-82	-121	18	12	15
424	353	167	-83	-57	-109	12	18	13
		173			-83			13
900 s								
254	164	86	-230	-160	-46	15	12	5
	167			-166			13	
194	145	58		-133 -152	-130	14	9	7
	209			-167			12	
216	184	2	-174	-137	-143	6	8	9
242	185	57	-169	-145	-148	5	4	11
255	230	16	-196	-112	-149	9	13	9
		28			-132			9
300 s								
28	8	106	-180	-105	-10	11	8	7
	25			-102			10	
61	35	74		-103 -114	-91	11	8	13
	78			-99			8	
66	77	-63	-121	-87	-116	8	8	11
87	65	-40	-130	-130	-103	7	8	13
95	65	-88	-138	-50	-107	12	26	10
		53			-80			7
67 s								
-46	3	65	-5	45	-85	16	10	10
	39			76			18	
99	-40	152		57 -31	-70	16	15	18
	78			62			16	
40	65	-255	-18	23	-100	14	23	16
41	71	-189	-51	-14	-82	13	12	16
51	137	-171	-46	36	11	14	31	11
		-69			33			10

Table 5. Transfer Functions for the Magnetometer Array (continued)

	Z_r^N				Z_i^N				2σ			
2700 s												
	-41	13		79	1	-18		1	17	14		6
		31				-2				14		
		83	104	109		-20	18	-18		15	11	7
		70				13				12		
		64	72	144		-22	8	11		12	12	12
		65	87	166		-15	3	-7		12	8	12
		-17	75	125		-22	-3	5		9	15	11
				77				-23				11
900 s												
	-64	-7		71	-10	-1		33	8	7		3
		32				-5				8		
		82	92	93		1	5	-7		8	6	5
		59				6				7		
		46	48	124		-4	7	-3		6	8	7
		52	84	141		-3	8	-4		5	8	8
		-46	68	104		1	30	-10		6	12	8
				44				-19				7
300 s												
	-40	4		132	-13	-12		74	7	6		5
		40				-28				8		
		94	118	147		-10	4	11		7	6	11
		77				0				6		
		65	71	147		-10	5	-9		5	6	11
		71	107	156		1	6	-7		4	6	10
		-25	113	104		17	42	-11		7	21	9
				50				-2				6
67 s												
	-75	-54		259	-42	-41		33	14	8		7
		-22				-58				15		
		29	78	113		-32	78	-52		13	12	17
		65				-13				16		
		29	-80	100		-26	-80	-76		11	19	14
		62	71	97		-28	-9	-54		10	11	14
		12	86	77		8	16	-34		11	30	11
				52				14				10
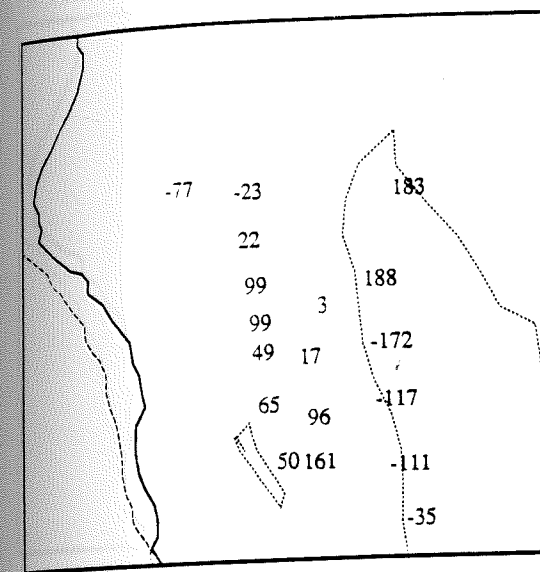
(a) T = 60 s and θ = 50°
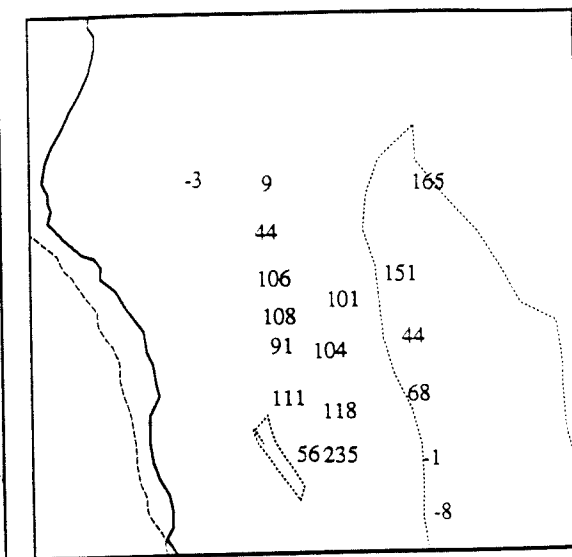
(b) T = 300 s and θ = 60°
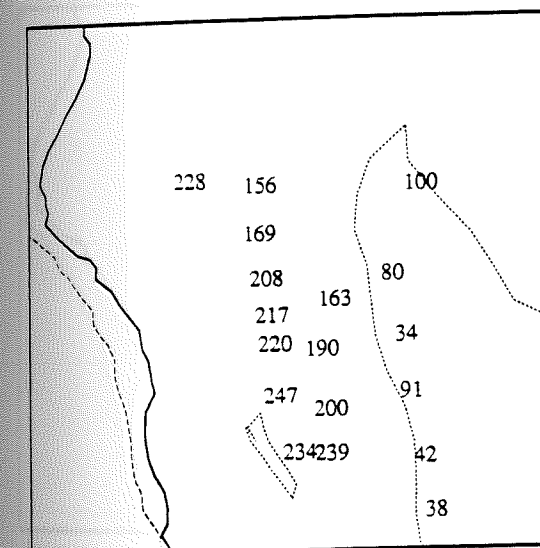
(c) T = 900 s and θ = 75°
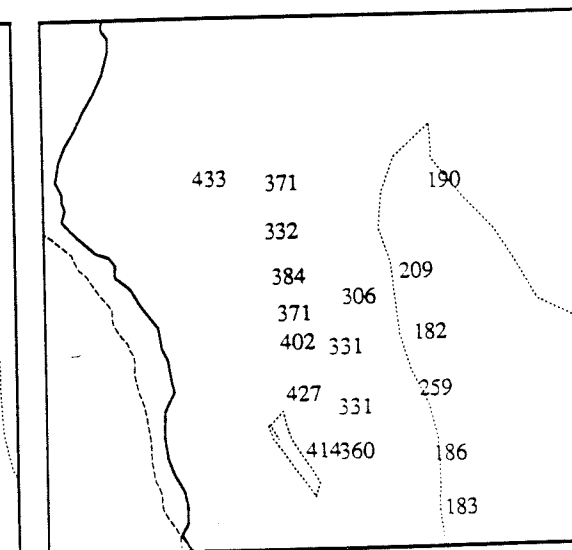
(d) T = 2700 s and θ = 80°

Figure 5.2.1 Real components of vertical magnetic field for a hypothetical unit source field directed at azimuth θ_s. Values of the optimal source field vary with period: (a) $\theta_s = 50°$; (b) $\theta_s = 60°$; (c) $\theta_s = 75°$; (d) $\theta_s = 80°$. These choices correspond to an attempted $E_\parallel$ mode analysis of the array.
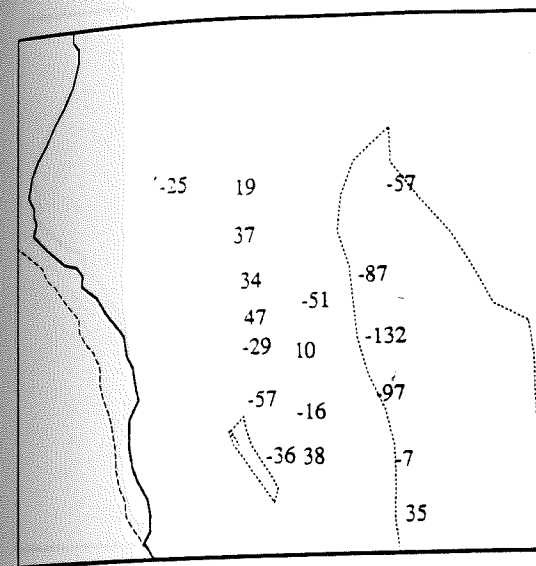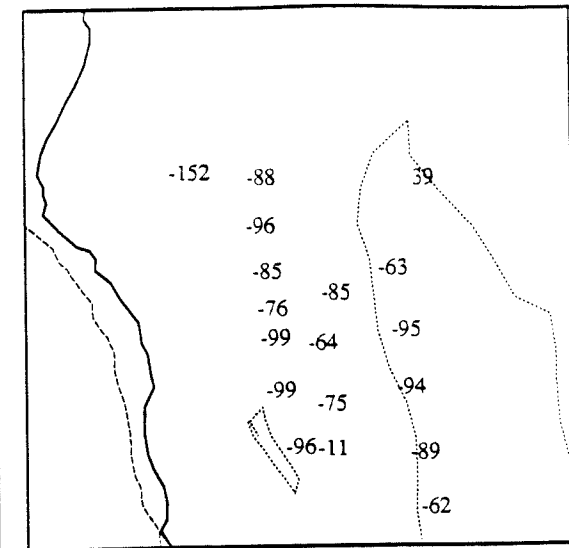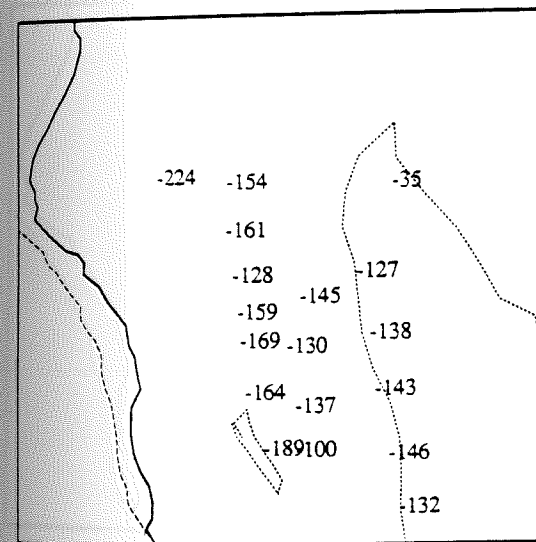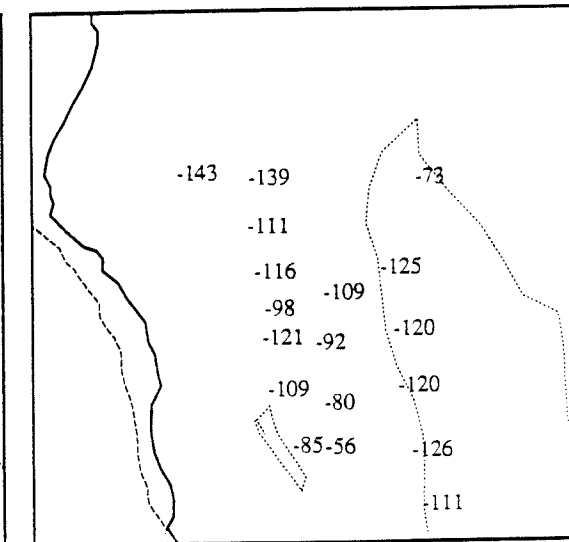
(a) T = 60 s and θ = 50°

(b) T = 300 s and θ = 60°

(c) T = 900 s and θ = 70°

(d) T = 2700 s and θ = 80°

Figure 5.2.2 Imaginary components of vertical magnetic field for a hypothetical unit source field directed at azimuth θ_s. Values of the optimal source field vary with period: (a) $\theta_s = 50°$; (b) $\theta_s = 60°$; (c) $\theta_s = 75°$; (d) $\theta_s = 80°$. These choices correspond to an attempted $E_{\parallel}$ mode analysis of the array.

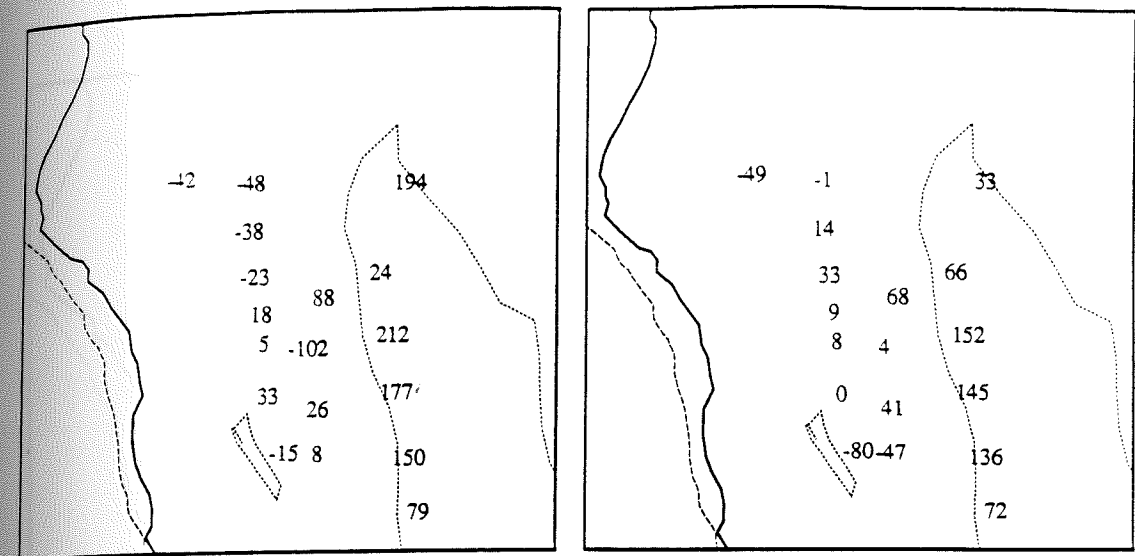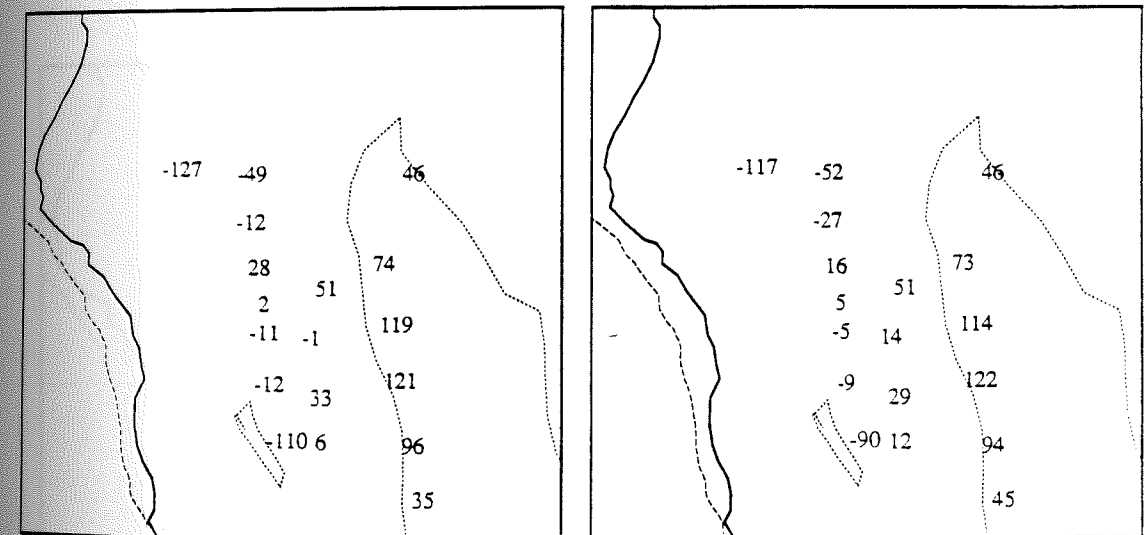(a) T = 60 s and θ = -40°

(b) T = 300 s and θ = -30°

(c) T = 900 s and θ = -15°

(d) T = 2700 s and θ = -10°

Figure 5.2.3 Real components of vertical magnetic field for a hypothetical unit source field directed at azimuth θ_s. Values of the optimal source field vary with period: (a) $\theta_s = -40°$; (b) $\theta_s = -30°$; (c) $\theta_s = -15°$; (d) $\theta_s = -10°$. These choices correspond to an attempted $E_\perp$ mode analysis of the array.

(a) T = 60 s and θ = -40°

(b) T = 300 s and θ = -30°

(c) T = 900 s and θ = -15°

(d) T = 2700 s and θ = -10°

Figure 5.2.4 Imaginary components of vertical magnetic field for a hypothetical unit source field directed at azimuth θ_s. Values of the optimal source field vary with period: (a) $\theta_s = -40°$; (b) $\theta_s = -30°$; (c) $\theta_s = -15°$; (d) $\theta_s = -10°$. These choices correspond to an attempted E_1 mode analysis of the array.
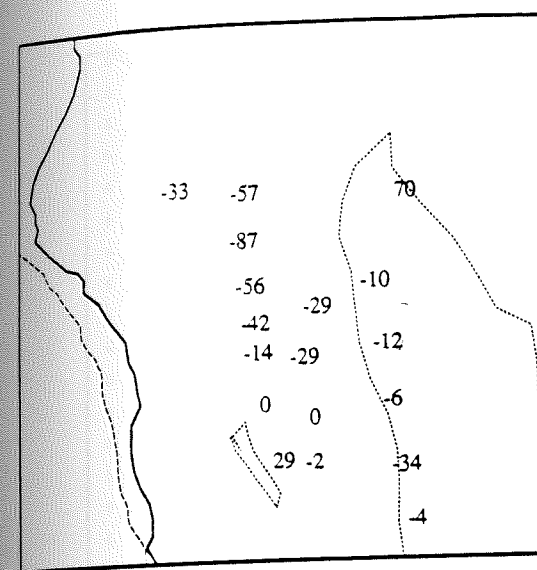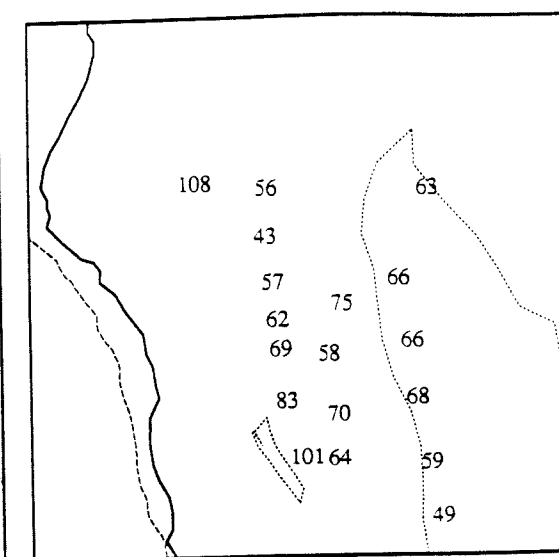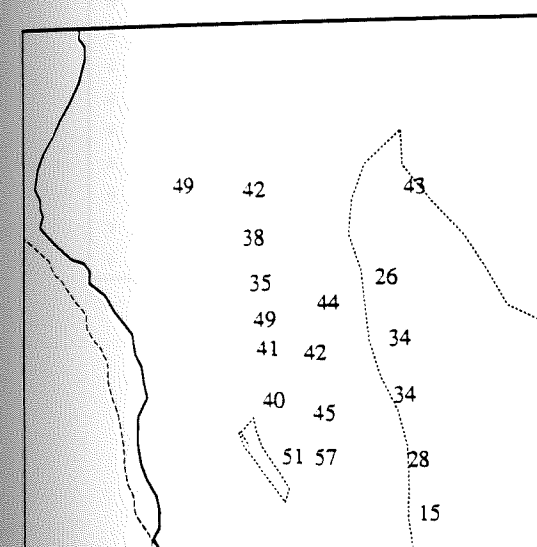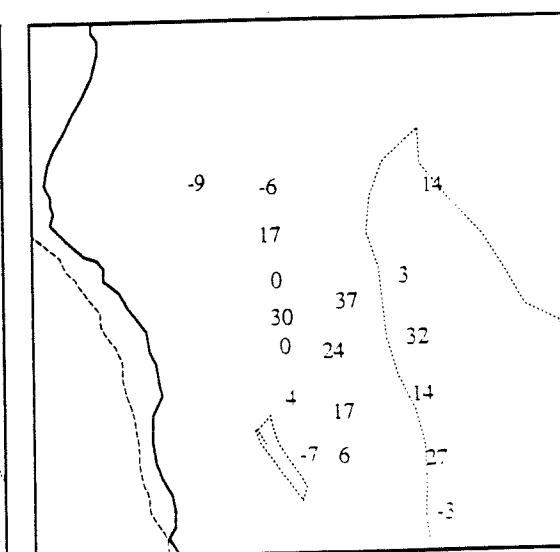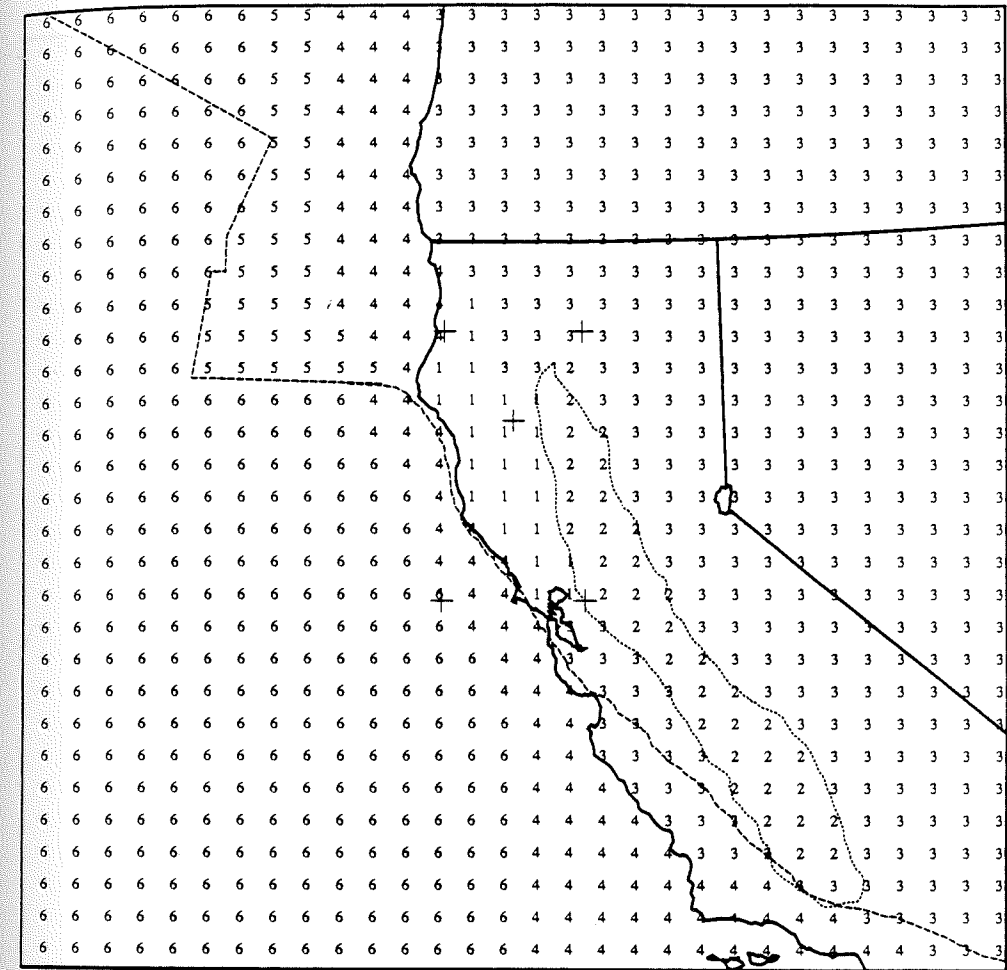
distance in kilometers

Figure 5.3.1 Conductivity structure for Model A. This model contains all of the surface features described in Table 3 except that all of the deep bathymetry past the continental shelf was changed to the constant value for 2000 m of seawater.

MM = 15
↓

LL = 16
→

R = 1.0

-200 -100 0 100 200
distance in kilometers

Figure 5.3.2(a) Real induction arrows are plotted for Model A. Arrows represent magnetic field values relative to the value at the upper right grid element (LL = 30, MM = 30). A constant vector of azimuth = 82.2547° and radius = 0.075320 was subtracted from all v_r.

MM = 15

↓

LL = 16

→

R = 1.0

-200   -100   0   100   200
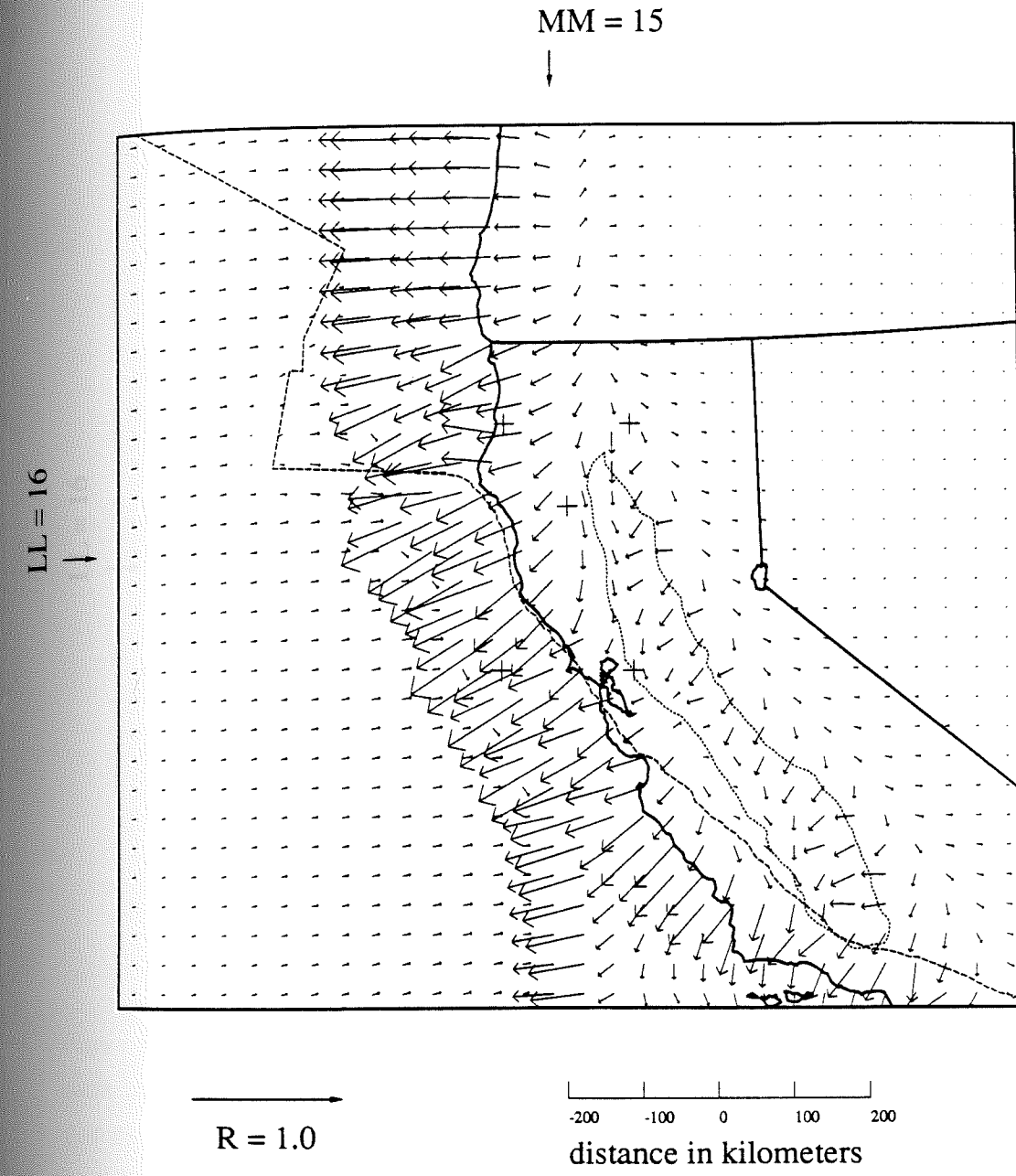
distance in kilometers
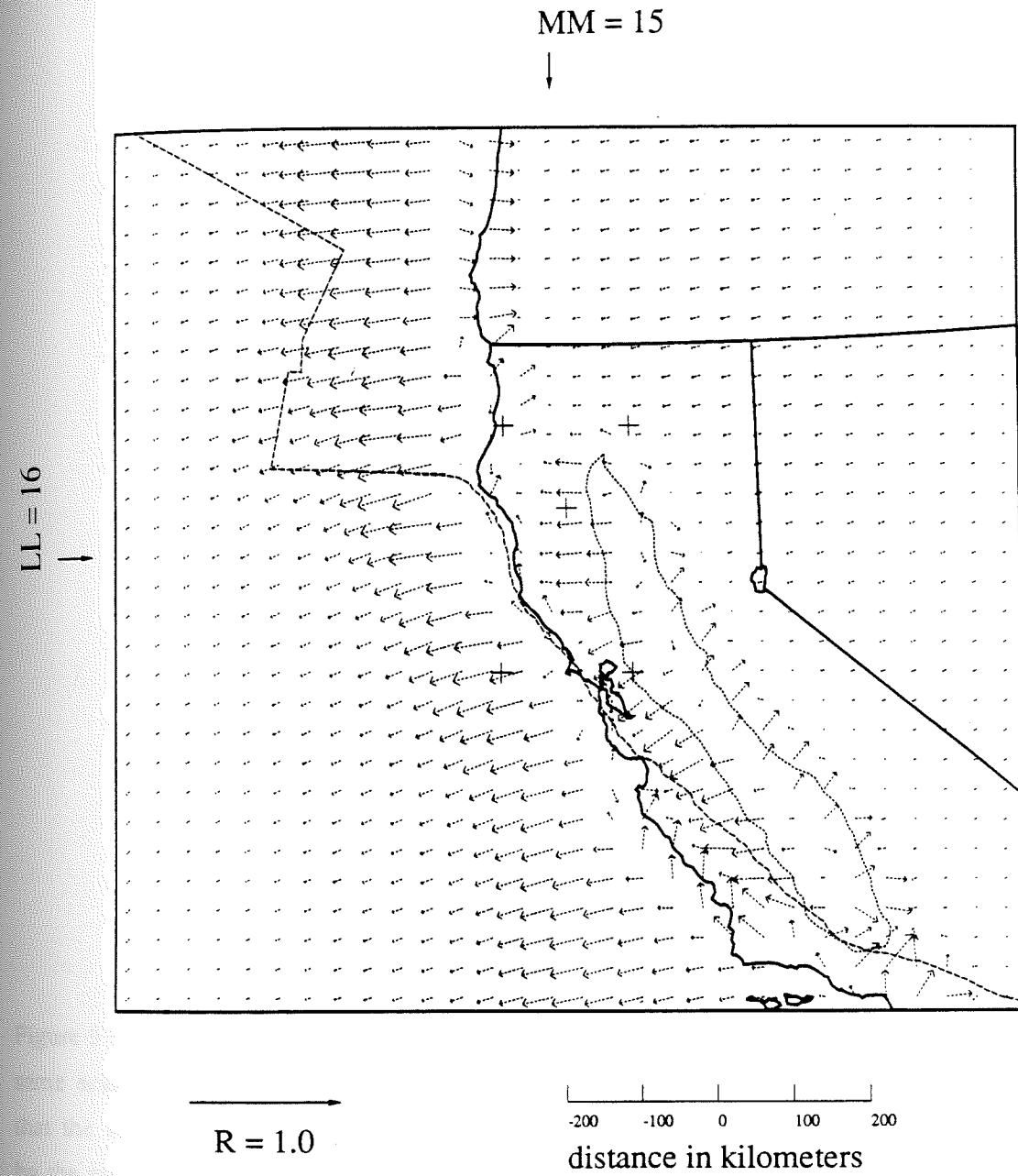
Figure 5.3.2(b) Imaginary induction arrows are plotted for Model A. Arrows represent magnetic field values relative to the value at the upper right grid element (LL = 30, MM = 30). A constant vector of azimuth = –104.9560° and radius = 0.0595339 was subtracted from all v_i.
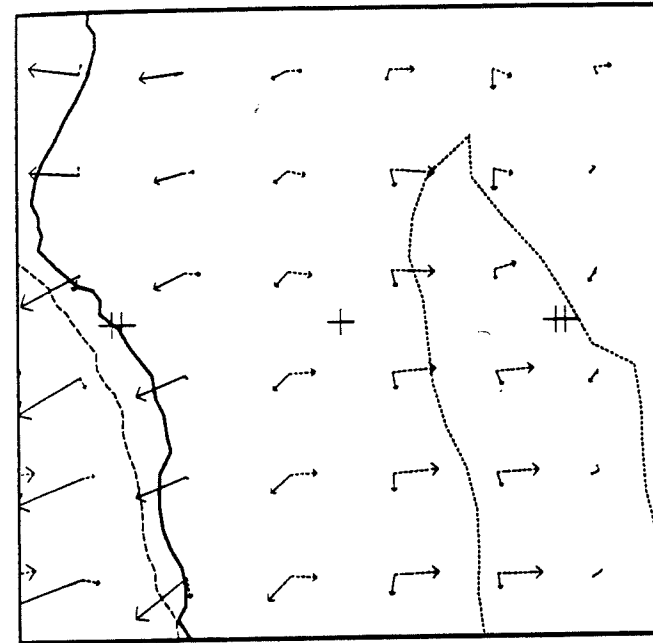
Figure 5.3.2(c) Both real (solid) and imaginary (dashed) induction arrows are plotted at the same scale as Figure 5.1.1. Comparison of the values from the model and the data show that the surface conductors alone reproduce many important features of the fields mapped by the array.

Figure 5.3.3 Vertical field response functions for a S - N traverse of the model at MM = 15, with a source polarization $\theta_s = 0°$. The traverse corresponds to the western profile of the magnetometer array and the origin is at 123° lon. and 40° lat.

51
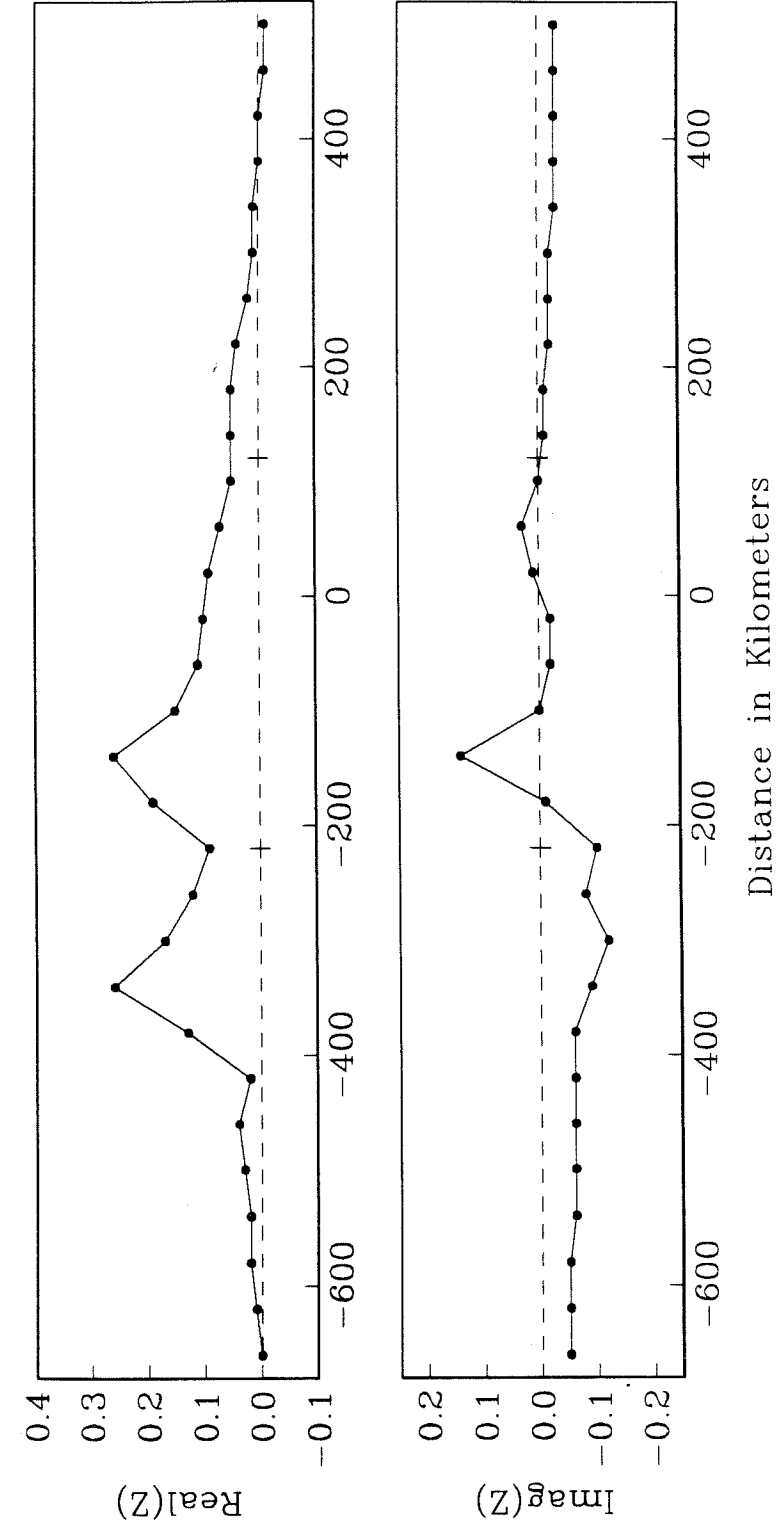
Figure 5.3.4 Vertical field response functions for a N - S traverse of the model at MM = 15, with a source polarization $\theta_s = -15°$.

Figure 5.3.5 Vertical field response functions for a W - E traverse of the model at LL = 16, with a source polarization $\theta_s = 0°$. The origin corresponds to the center of the magnetometer array at 123° lon. and 40° lat.

Figure 5.3.6 Vertical field response functions for a W - E traverse of the model at LL = 16, with a source polarization $\theta_s = -15°$. The origin corresponds to the center of the magnetometer array at 123° lon. and 40° lat.
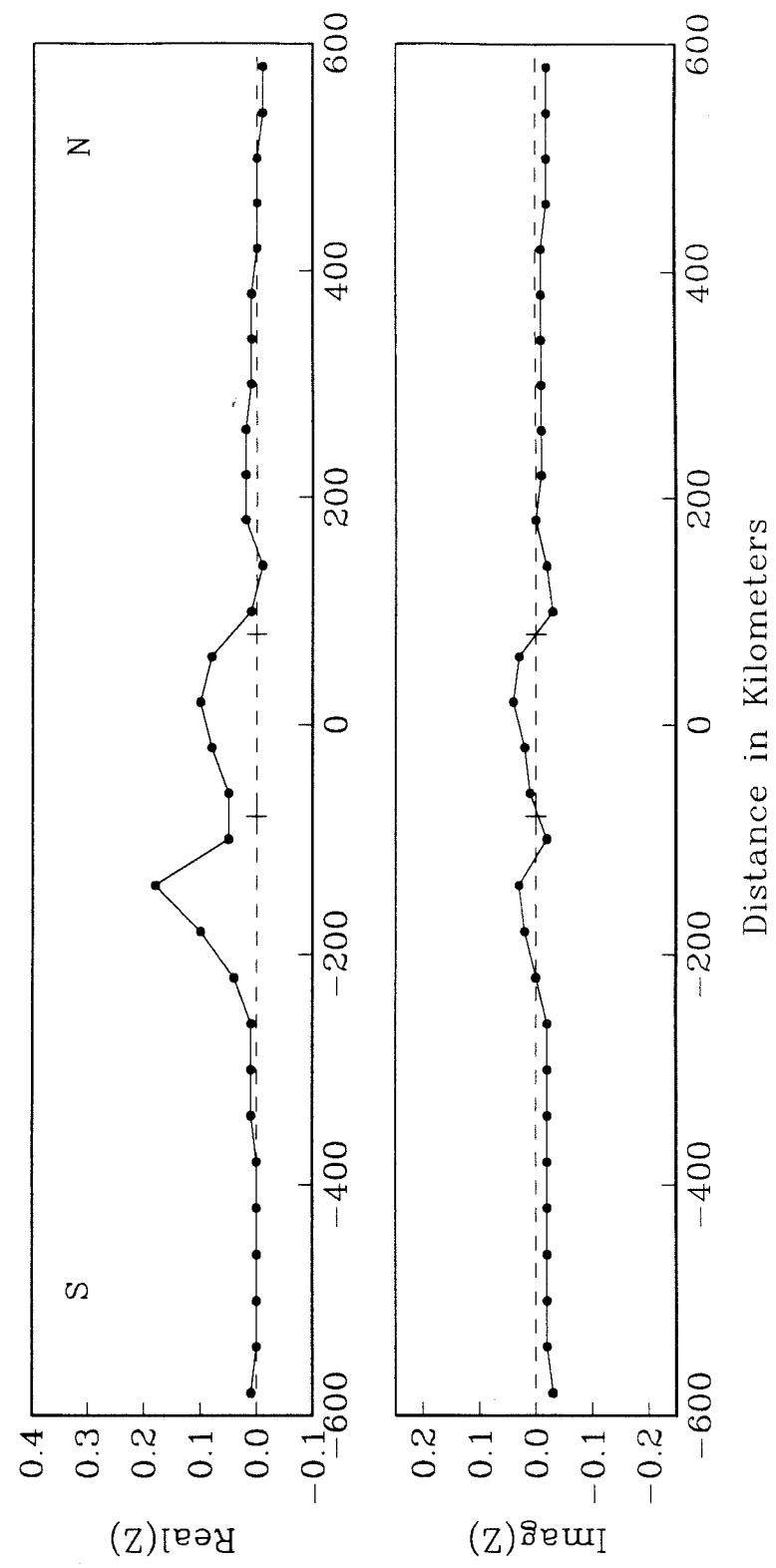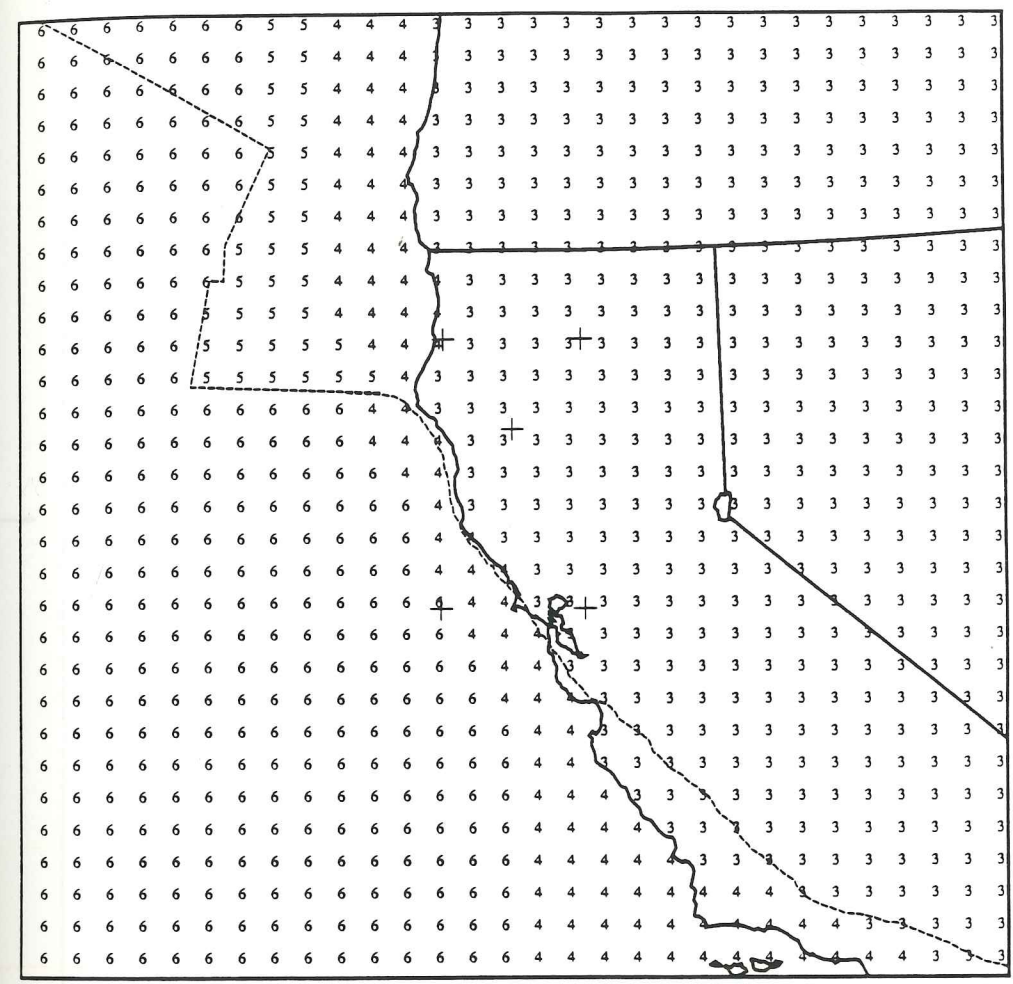
-200   -100   0   100   200

distance in kilometers

Figure 5.3.7 Conductivity structure for Model B. This model shows the effects of the irregular coastline with the bathymetry and a homogeneous continental crust included.

MM = 15

↓

LL = 16 →

R = 1.0

-200 -100 0 100 200

distance in kilometers

Figure 5.3.8(a) Real induction arrows are plotted for Model B. Arrows represent magnetic field values relative to the value at the upper right grid element (LL = 30, MM = 30). A constant vector of azimuth = 82.6597° and radius = 0.0771261 was subtracted from all v_r.

MM = 15
↓

LL = 16 →

R = 1.0

-200   -100   0   100   200

distance in kilometers

Figure 5.3.8(b) Imaginary induction arrows are plotted for Model B. Arrows represent magnetic field values relative to the value at the upper right grid element (LL = 30, MM = 30). A constant vector of azimuth = −103.6890° and radius = 0.0571905 was subtracted from all v_i.

57

Real(Z)

Imag(Z)

Distance in Kilometers

Figure 5.3.9 Vertical field response functions for a W - E traverse of model B at LL = 16, with a source polarization $\theta_s = -15°$. The dogleg bend in the coastline occurs 60 km south of this traverse at Point Cabrillo and continues to the south.

58

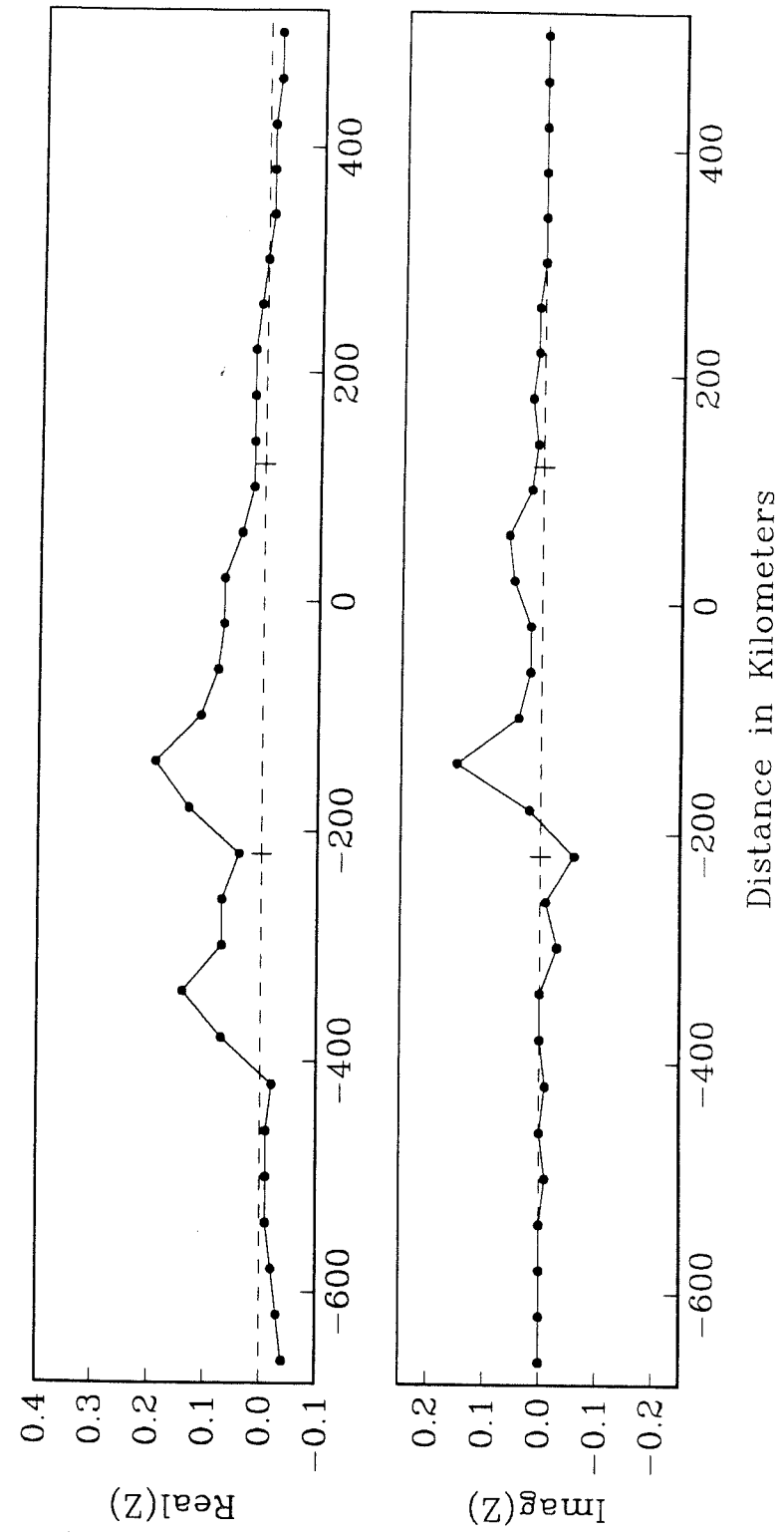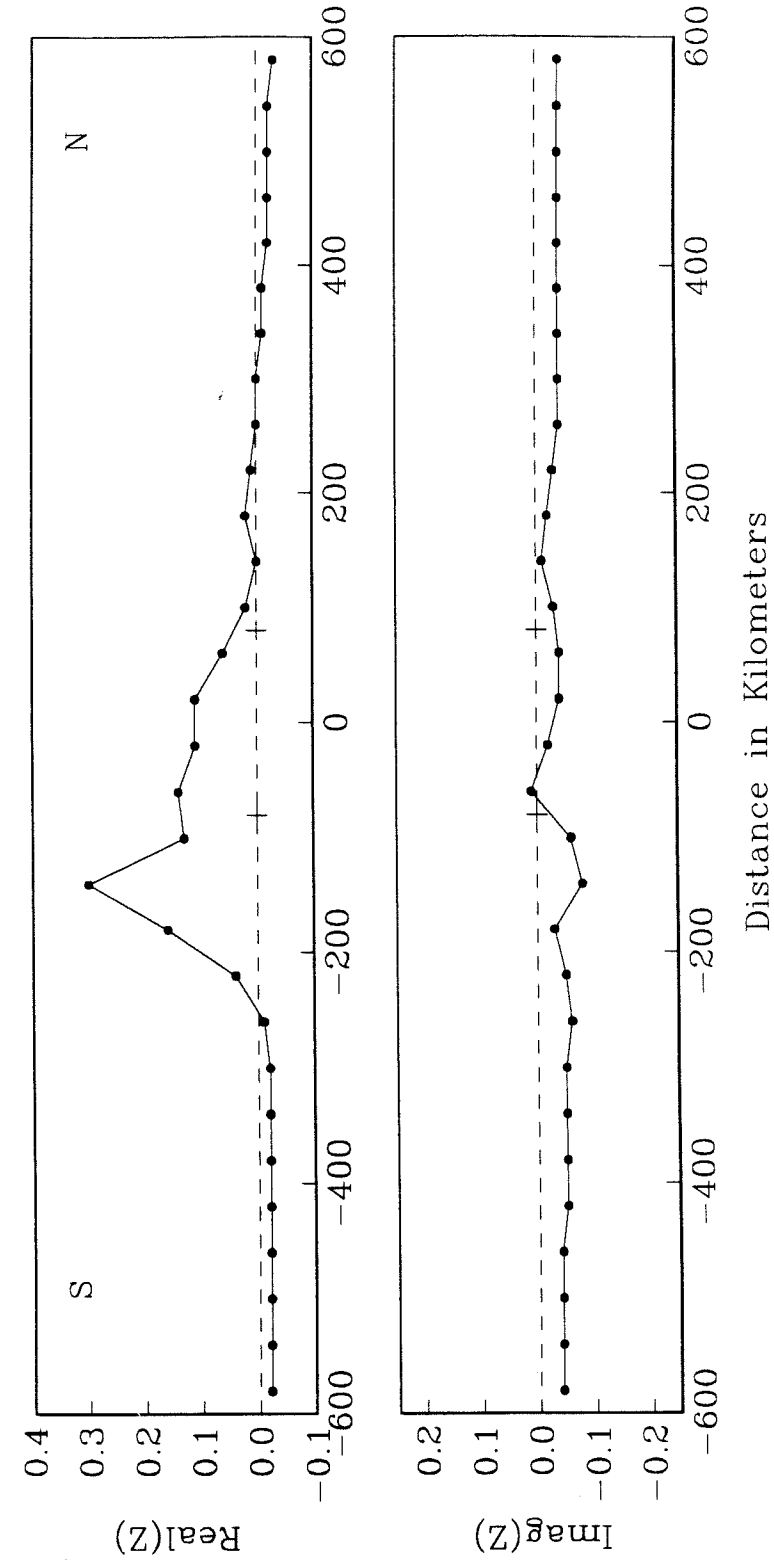Figure 5.3.10 Vertical field response functions for a N - S traverse of the model at MM = 15, with a source polarization $\theta_s = -15°$. The traverse corresponds to the western profile of the magnetometer array and the origin is at 123° lon. and 40° lat.

```
7 7 7 7 7 7 7 6 6 6 6 6 4 4 | 3 3 3 3 3 3 3 3 3 3 3 3 3 3 3 3
7 7 7 7 7 7 7 6 6 6 6 6 4 4 | 3 3 3 3 3 3 3 3 3 3 3 3 3 3 3 3
7 7 7 7 7 7 7 6 6 6 6 6 4 4 | 3 3 3 3 3 3 3 3 3 3 3 3 3 3 3 3
7 7 7 7 7 7 7 6 6 6 6 6 4 4 | 3 3 3 3 3 3 3 3 3 3 3 3 3 3 3 3
7 7 7 7 7 7 7 6 6 6 6 6 4 4 | 3 3 3 3 3 3 3 3 3 3 3 3 3 3 3 3
7 7 7 7 7 7 7 6 6 6 6 6 4 4 | 3 3 3 3 3 3 3 3 3 3 3 3 3 3 3 3
7 7 7 7 7 7 7 6 6 6 6 6 4 4 | 3 3 3 3 3 3 3 3 3 3 3 3 3 3 3 3
7 7 7 7 7 7 7 6 6 6 6 6 4 4 | 3 3 3 3 3 3 3 3 3 3 3 3 3 3 3 3
7 7 7 7 7 7 7 6 6 6 6'6 4 4 | 3 3 3 3 3 3 3 3 3 3 3 3 3 3 3 3
7 7 7 7 7 7 7 6 6 6 6 6 4 4 | 3 3 3 3 3 3 3 3 3 3 3 3 3 3 3 3
7 7 7 7 7 7 7 6 6 6 6 6 4 4 | 3 3 3 3 3 3 3 3 3 3 3 3 3 3 3 3
7 7 7 7 7 7 7 6 6 6 6 6 4 4 | 3 3 3 3 3 3 3 3 3 3 3 3 3 3 3 3
7 7 7 7 7 7 7 6 6 6 6 6 4 4 | 3 3 3 3 3 3 3 3 3 3 3 3 3 3 3 3
7 7 7 7 7 7 7 6 6 6 6 6 + 4 |3+3 3+3 3 3 3 3 3 3 3 3 3 3 3 3
7 7 7 7 7 7 7 6 6 6 6 6 4 4 | 3 3 3 3 3 3 3 3 3 3 3 3 3 3 3 3
7 7 7 7 7 7 7 6 6 6 6 6 4 4 | 3 3 2 2 2 3 3 3 3 3 3 3 3 3 3 3
7 7 7 7 7 7 7 6 6 6 6 6 4 4 |+3 3 2 2 2 3 3 3 3 3 3 3 3 3 3 3
7 7 7 7 7 7 7 6 6 6 6 6 4 4 | 3 3 2 2 2 3 3 3 3 3 3 3 3 3 3 3
7 7 7 7 7 7 7 6 6 6 6 6 4 4 | 3 3 2 2 2 3 3 3 3 3 3 3 3 3 3 3
7 7 7 7 7 7 7 6 6 6 6 6 4 4 | 3 3 2 2 2 3 3 3 3 3 3 3 3 3 3 3
7 7 7 7 7 7 7 6 6 6 6 6 4 4 | 3 3 2 2 2 3 3 3 3 3 3 3 3 3 3 3
7 7 7 7 7 7 7 6 6 6 6 6 + 4 | 3 3 2+2 2 3 3 3 3 3 3 3 3 3 3 3
7 7 7 7 7 7 7 6 6 6 6 6 4 4 | 3 3 2 2 2 3 3 3 3 3 3 3 3 3 3 3
7 7 7 7 7 7 7 6 6 6 6 6 4 4 | 3 3 2 2 2 3 3 3 3 3 3 3 3 3 3 3
7 7 7 7 7 7 7 6 6 6 6 6 4 4 | 3 3 2 2 2 3 3 3 3 3 3 3 3 3 3 3
7 7 7 7 7 7 7 6 6 6 6 6 4 4 | 3 3 2 2 2 3 3 3 3 3 3 3 3 3 3 3
7 7 7 7 7 7 7 6 6 6 6 6 4 4 | 3 3 2 2 2 3 3 3 3 3 3 3 3 3 3 3
7 7 7 7 7 7 7 6 6 6 6 6 4 4 | 3 3 2 2 2 3 3 3 3 3 3 3 3 3 3 3
7 7 7 7 7 7 7 6 6 6 6 6 4 4 | 3 3 2 2 2 3 3 3 3 3 3 3 3 3 3 3
```

```
|___|____|____|____|____|
-200  -100   0   100  200
```

distance in kilometers

Figure 5.3.11 Conductivity structure for Model C. This model is basically two dimen-sional, showing the effects of the coastal edge anomaly with the deep bathymetry and a truncated Central Valley included.

MM = 15

↓

LL = 13

→

R = 1.0

-200 -100 0 100 200
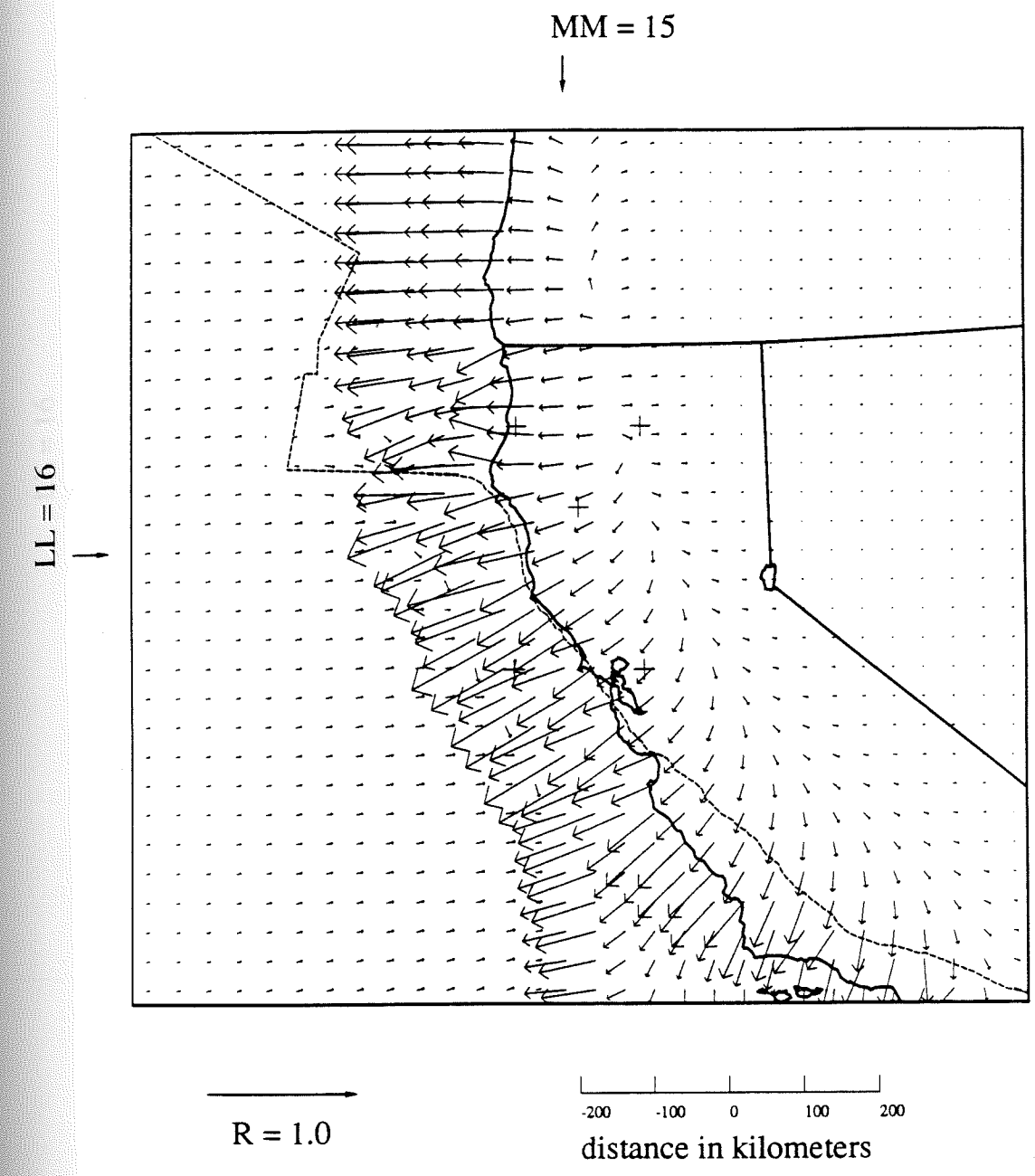
distance in kilometers
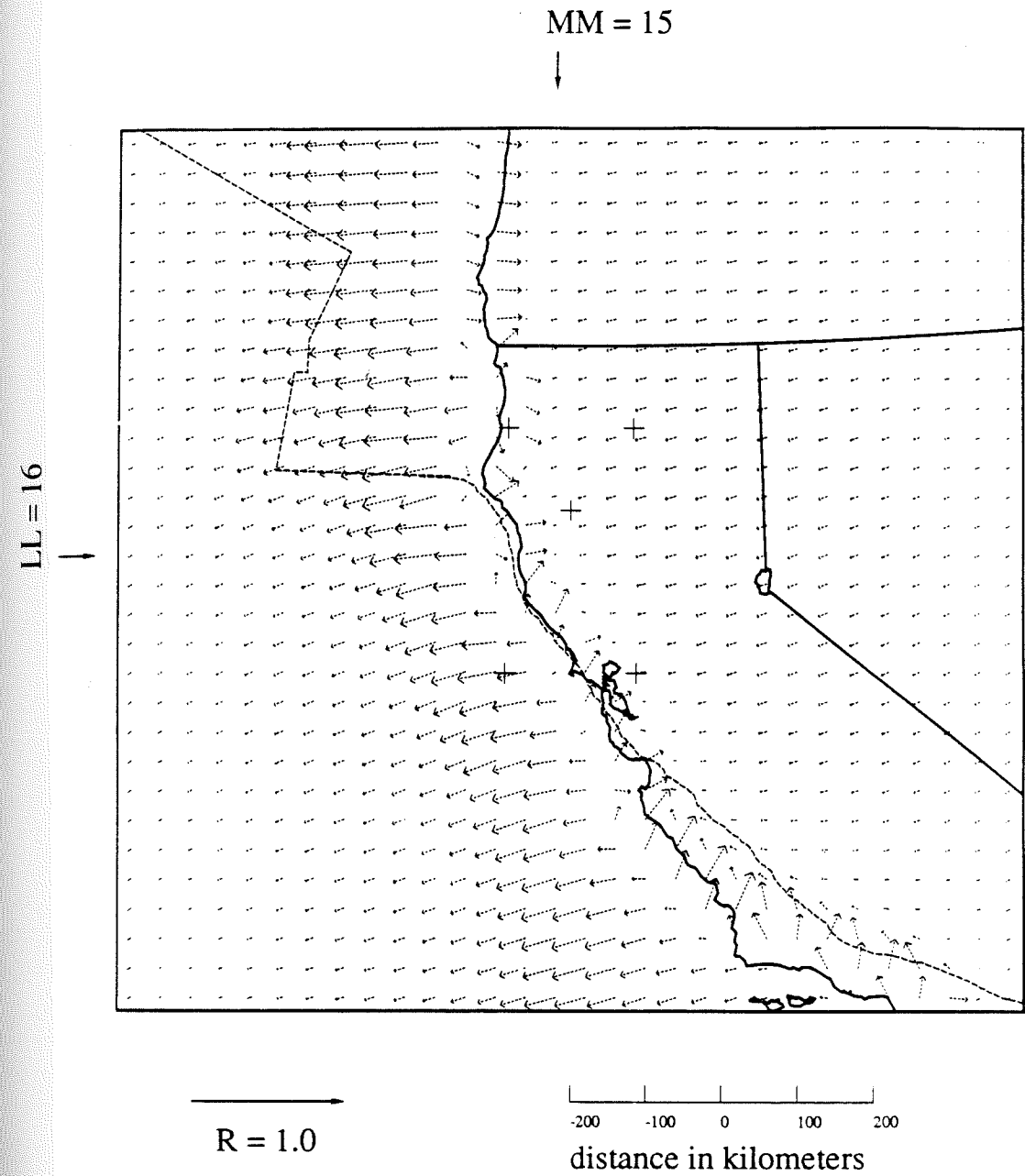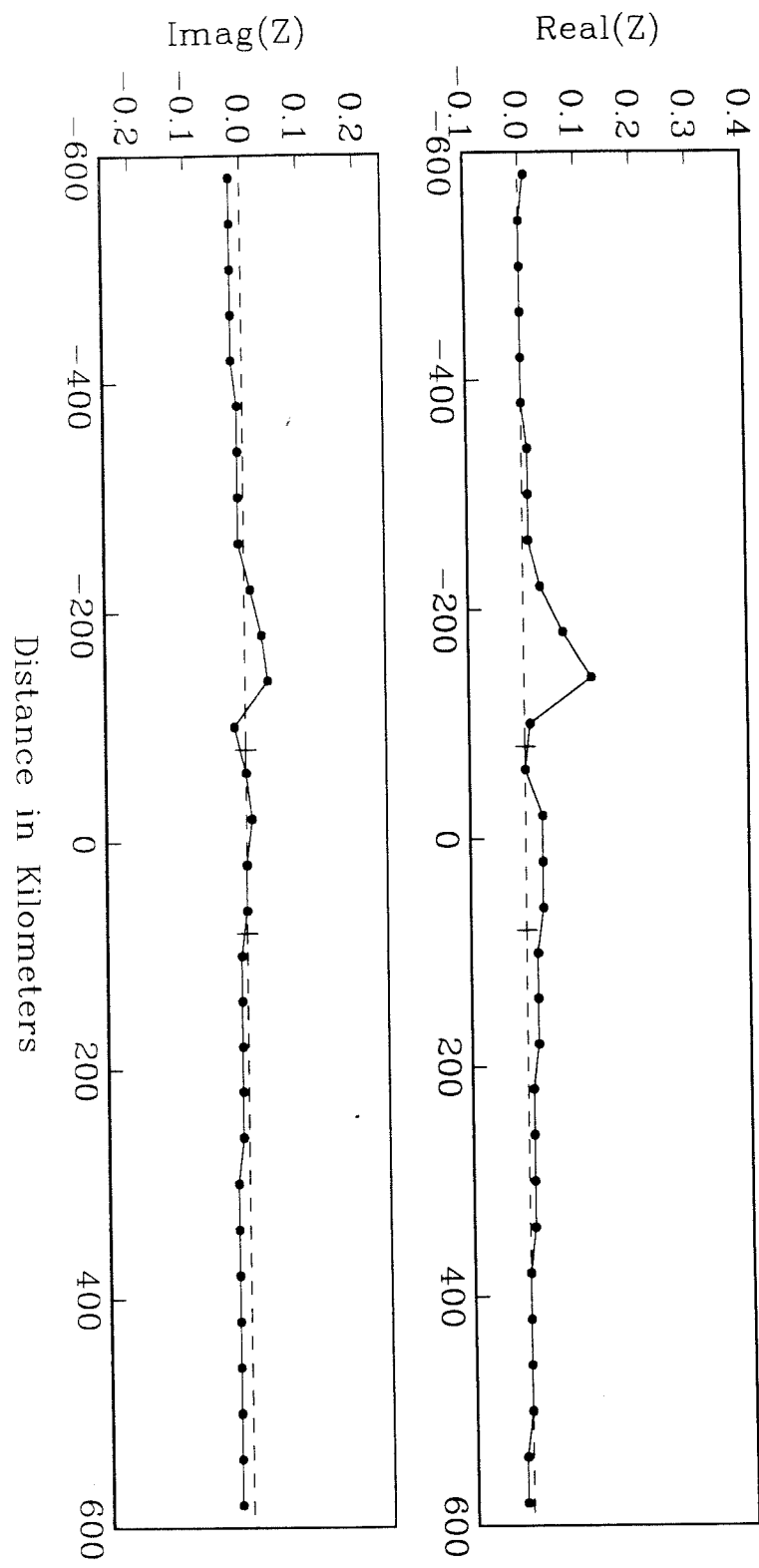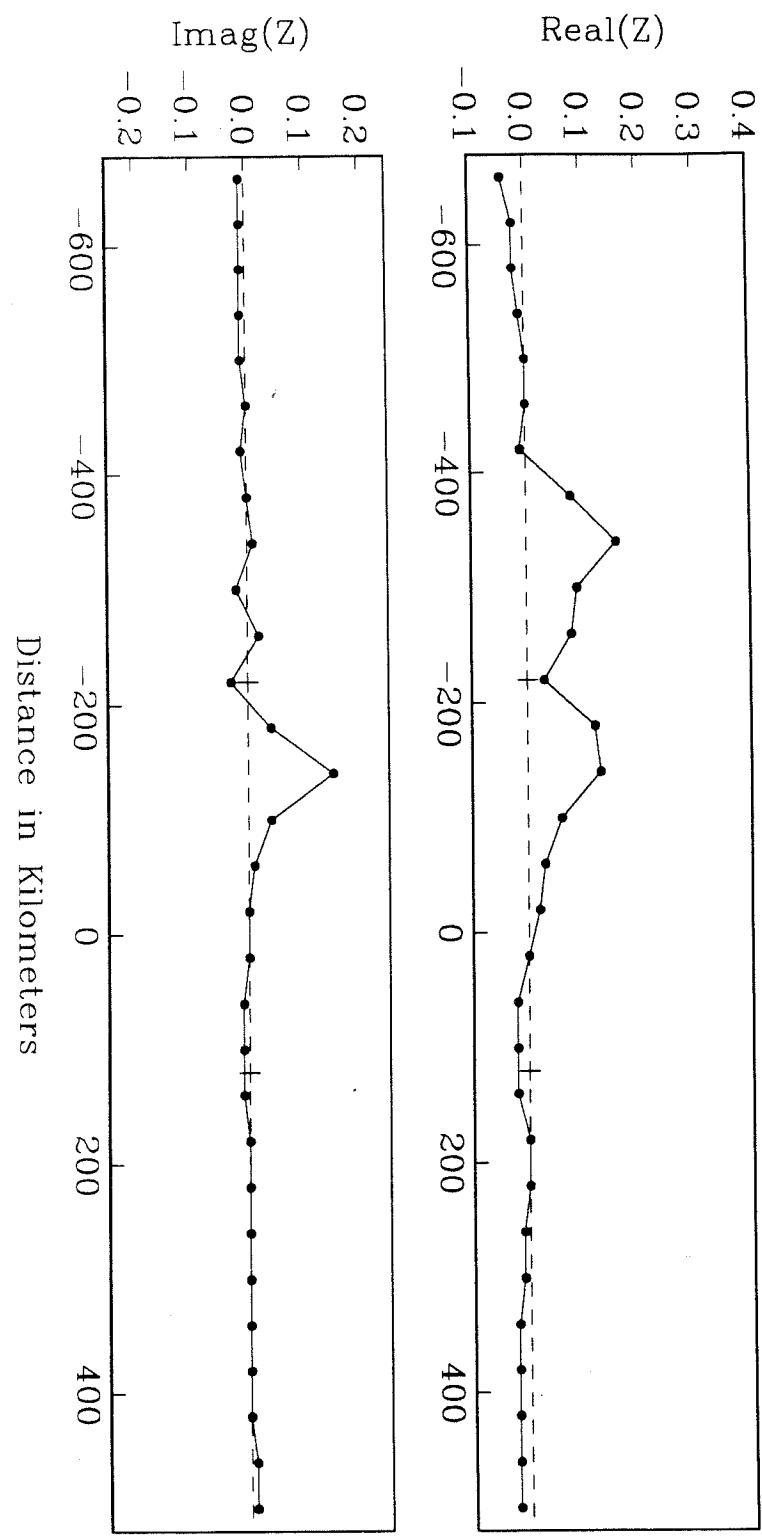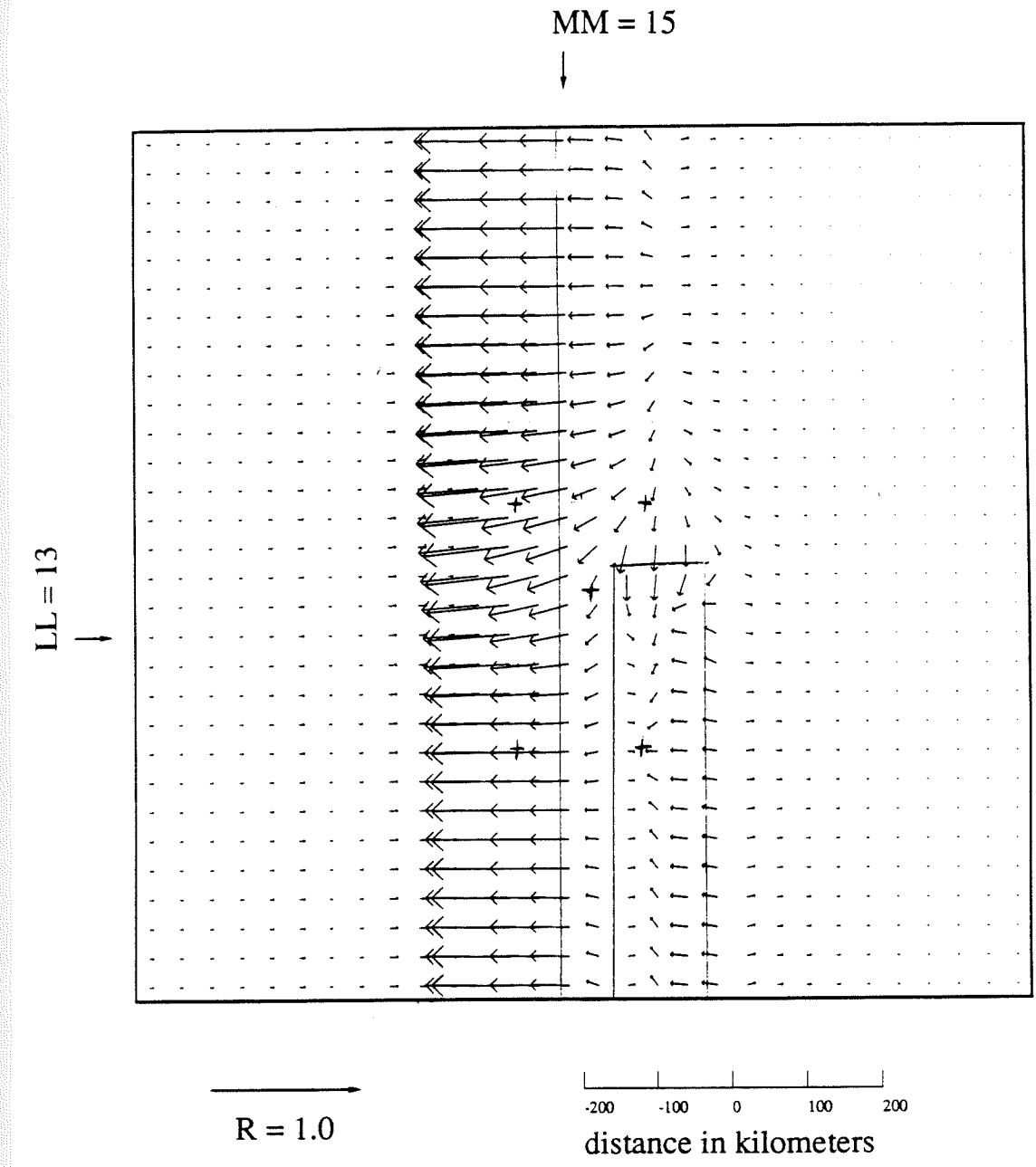
Figure 5.3.12(a) Real induction arrows are plotted for Model C. Arrows represent magnetic field values relative to the value at the upper right grid element (LL = 30, MM = 30). A constant vector of azimuth = 87.0488° and radius = 0.0762211 was subtracted from all v_r.

MM = 15

LL = 13

R = 1.0

distance in kilometers

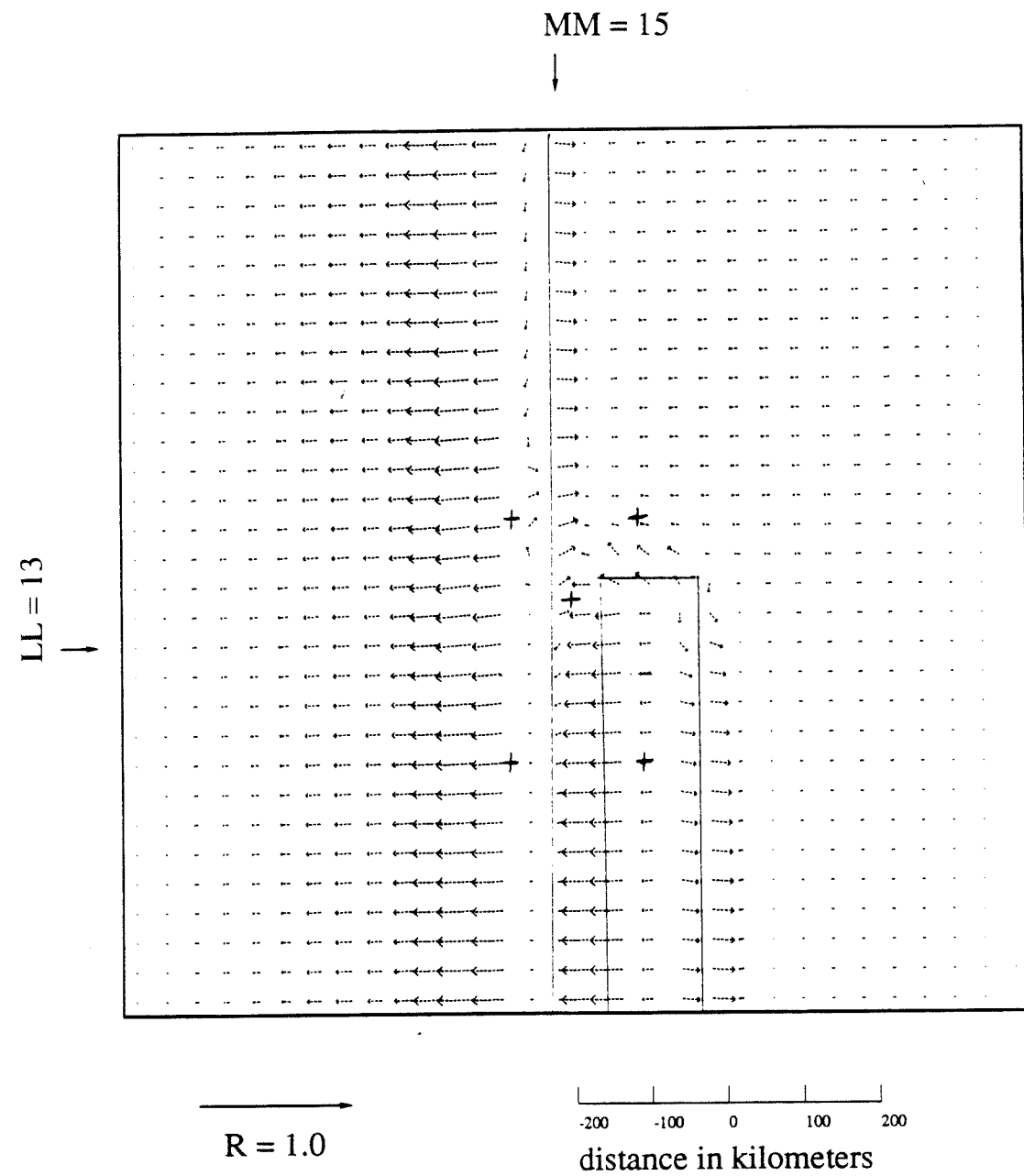-200   -100   0   100   200

Figure 5.3.12(b) Imaginary induction arrows are plotted for Model C. Arrows represent magnetic field values relative to the value at the upper right grid element (LL = 30, MM = 30). A constant vector of azimuth = –92.7677° and radius = 0.0597764 was subtracted from all v_i.

Figure 5.3.13 Vertical field response functions for a N - S traverse of model C at MM = 15, with a source polarization $\theta_s = 15°$. The traverse corresponds to the western profile of the magnetometer array and the origin is at 123° lon. and 40° lat.
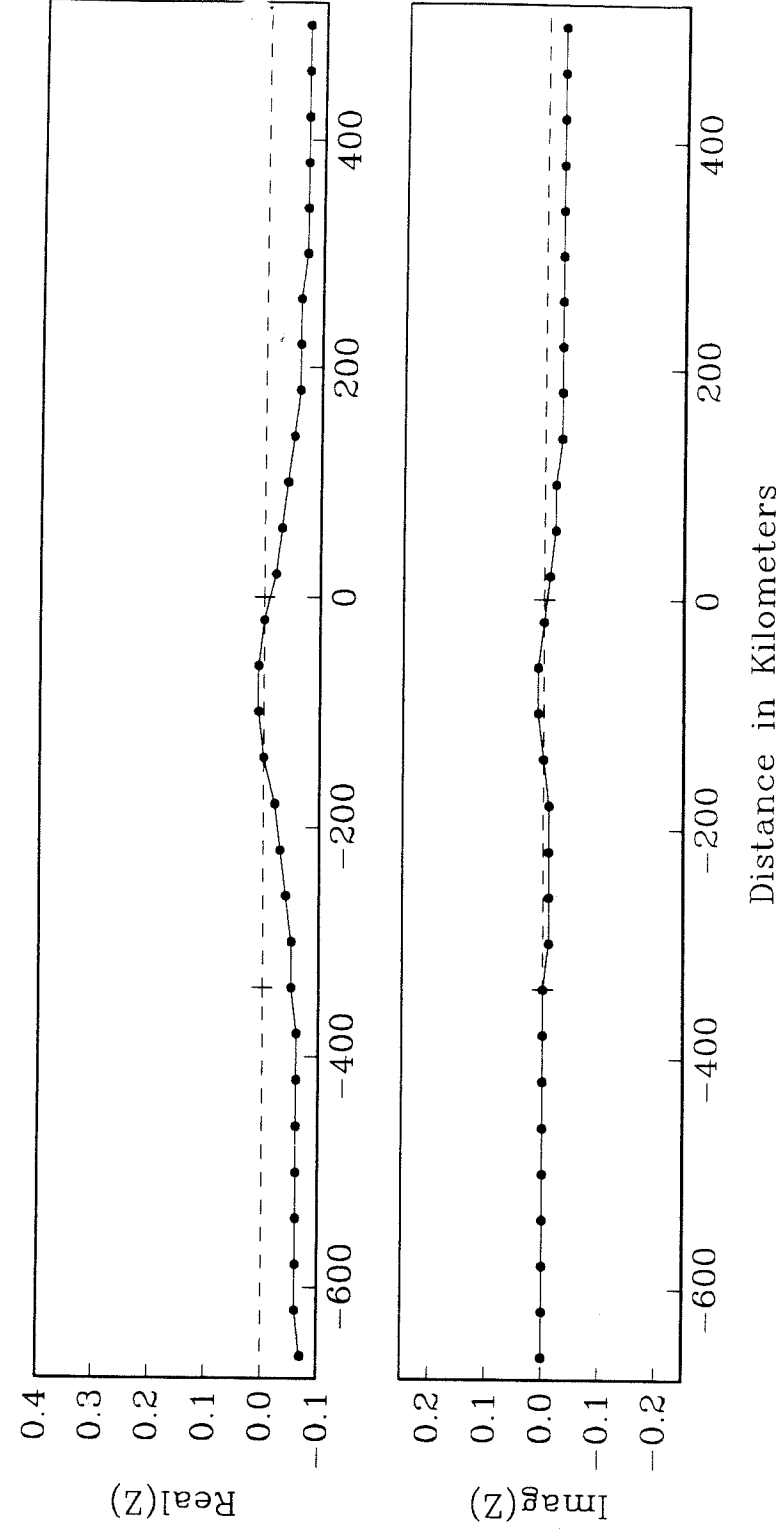
63

Figure 5.3.14 Vertical field response functions for a W - E traverse of model C at LL = 13, with a source polarization $\theta_s = 15°$. The linear valley was truncated above LL = 15, 80 km north of this traverse which corresponds to a transect across the center of the array.

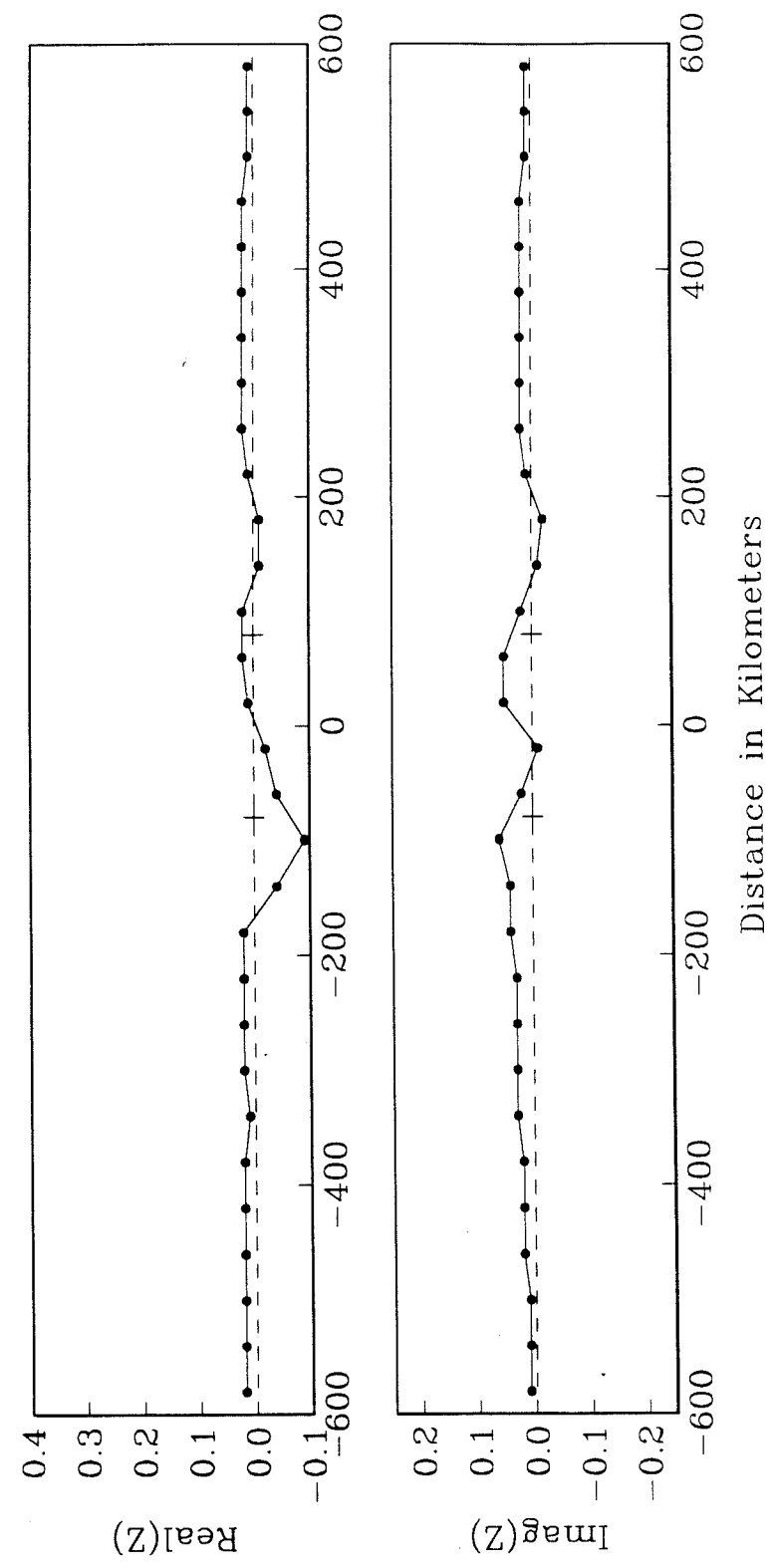Distance in Kilometers

Table 6. Optimal Source Polarizations for Four Period Bands

Period	θ_s
60	-40
300	-30
900	-15
2700	-10

CHAPTER 6

CONCLUSIONS

Study of the vertical field response indicates that a rigorous two-dimensional interpretation of the array requires the use of a different source polarization for each period band. If there were an anomaly associated with the Gorda Plate edge, then the best opportunity to detect it would be in the plot of the minimum response curves derived from the hypothetical event analyses of section 5.2. Presumably, at least the strongest surface signal, that of the coastal edge, has been minimized for the optimal source polarizations.

Figure 6.1.1 shows plots of the real and imaginary transfer functions along the westmost profile from the hypothetical event analyses presented in section 5.2. Data points from POT, the southmost station of the profile, have been included but are suspect because of the strong localized fields due to surface cover at the site. Comparison of Real(Z) values with the errors shown in Table 6 show that the Real(Z) variations in the center of the array are within the error limits of the long period data. Except for the possibly anomalous endpoints, there is little anomalous field left in this profile. It is interesting to compare this attempt at an $E_\perp$ mode interpretation with the results from a two-dimensional model of a step in the asthenosphere shown in Figure 6.1.2. Important qualitative differences exist between these two sets of response functions. Values of Real(Z) from the two-dimensional step model are always positive in contrast to the large negative values seen at both ends of the array profile. Model values are more frequency dependent than the data as well.

Differences between the data and the model results are more distinct in the imaginary component of Z. Imag(Z) values from the data are: 1)uniformly positive except for two points; 2)show a significant increase in magnitude with period; and 3) display no symmetry along the profile. Values of Imag(Z)from the two-dimensional model differ from the array data in all of these regards: 1)negative values within 30 to 50 km of the step in deeper conductor; 2)virtual frequency independence; and 3) a symmetric bell shape centered on the origin. The imaginary component of the vertical field is most sensitive to the vertical conductivity structure in a conducting medium. Thus these qualitative distinctions between the

model and the data reveal a poor fit of a step in the asthenosphere to the array results.

All of these differences support the conclusion that no deep lying conductivity anomaly was detected by the magnetometer array. Reasonable estimates of anomalous fields from the surface conductors suffice to explain the direction and size of induction arrows calculated from the array data.

The most important recommendation from this study is the use of the three-dimensional modeling program in the design of future GDS or MT experiments. If the program had been readily accessible before this study then the complication resulting from the many surface conductors would have been considered in the station deployment. We would not have deployed the eastern and middle lines of the array. The equipment would have been put to better use by increasing the station density of the western line. Or a long (500-700 km) transect perpendicular to the ideal coastline could have been used to remove the coastal edge anomaly as was done by Everett and Hyndeman in southwestern Australia.

The thinsheet modeling programs are now readily accessible to the scientific community through the San Diego Supercomputing Center. Their use is highly recommended to improve future GDS or MT experiment design and interpretation.

67

Figure 6.1.1 Real(Z) and Imag(Z) are plotted versus distance relative to the origin at 40°
lat. Z values at each period were calculated for the optimal source polarization for an E_1
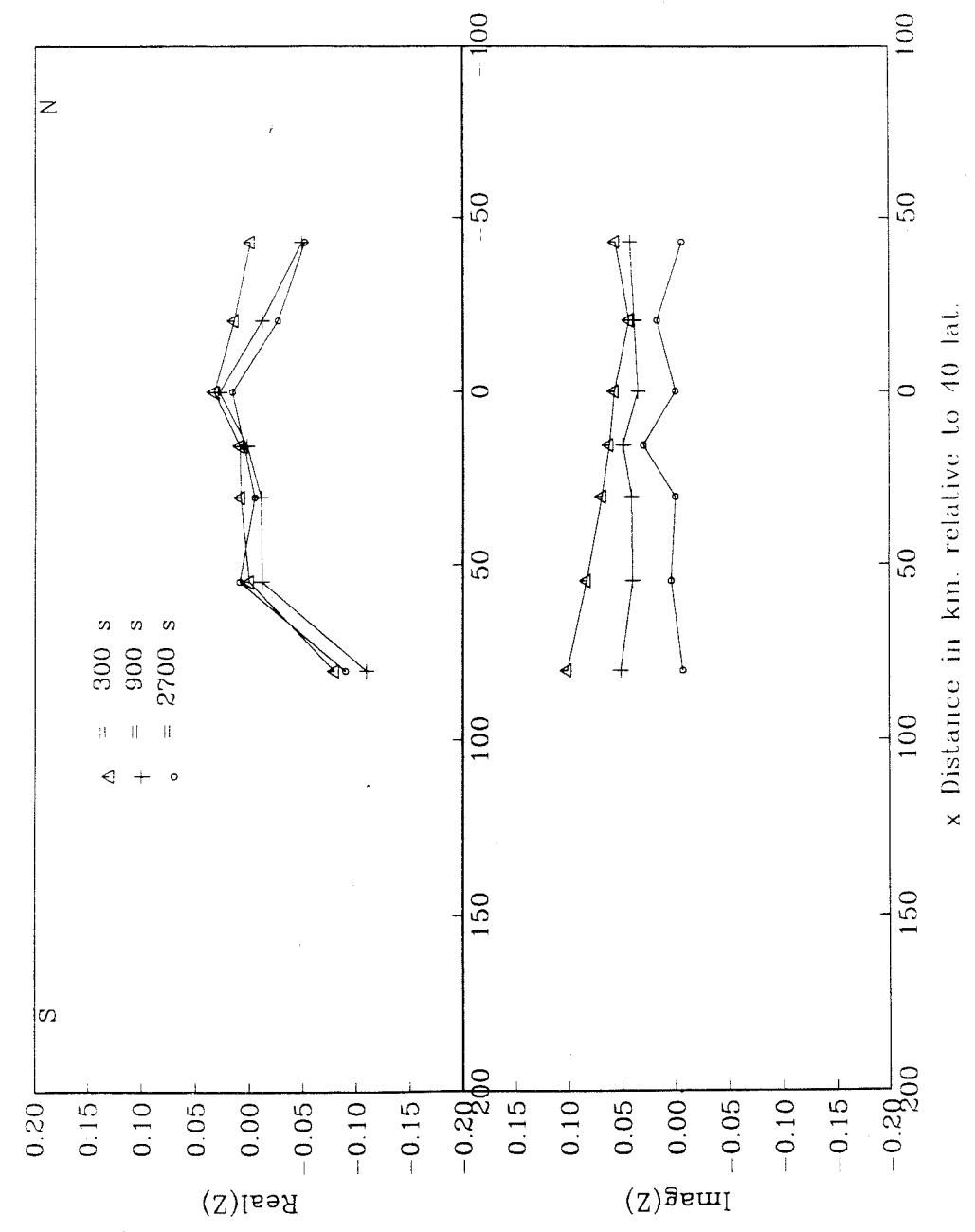interpretation.

68
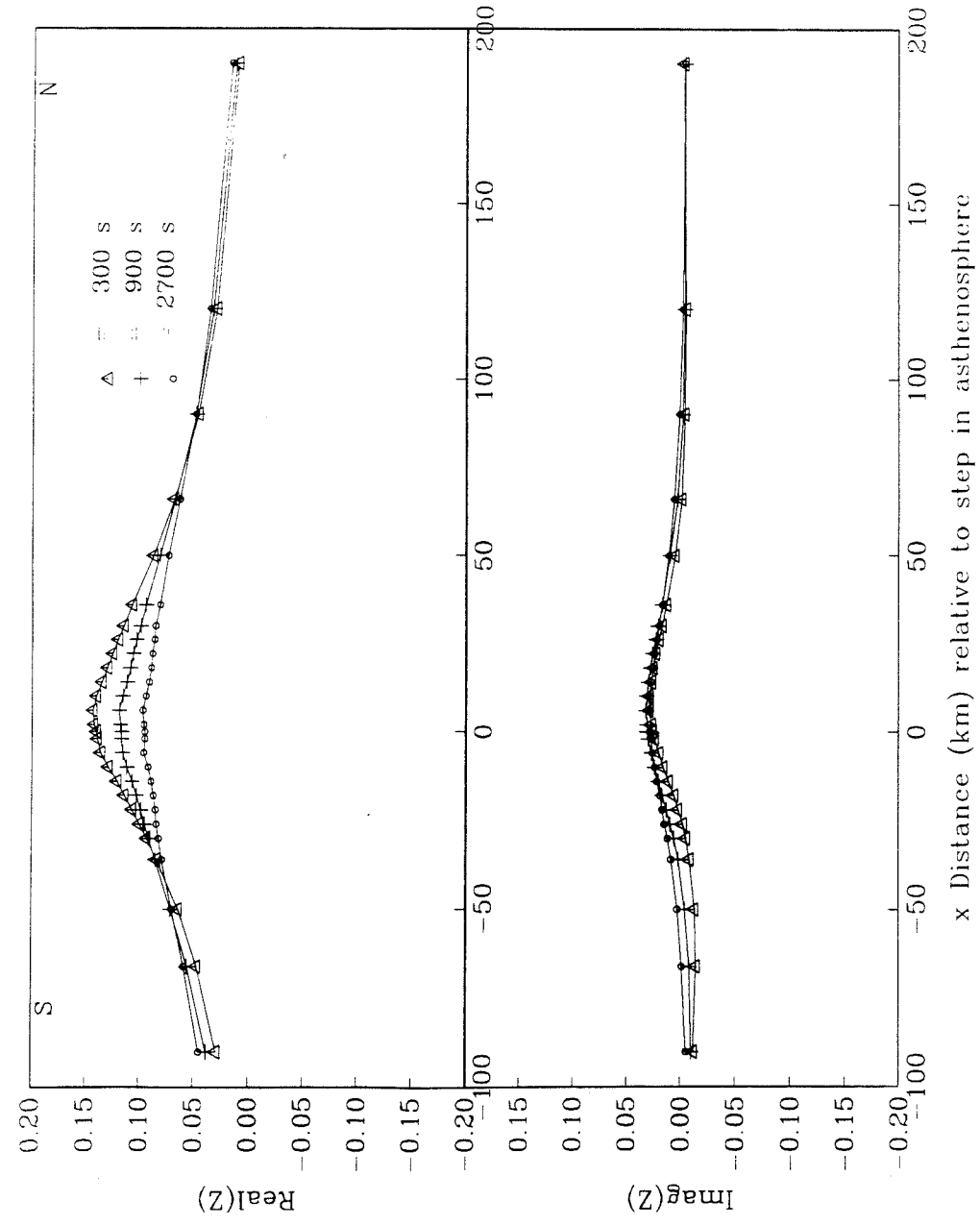

Figure 6.1.2 Real(Z) and Imag(Z) are plotted versus distance relative to the location of a 20 km step in the basal conductor. Z values were calculated from a two-dimensional model with two layers. The upper layer has σ = .001 S/m and the basal layer has σ = 0.1 S/m.

References

Bailey, R. C., Edwards, R. N., Garland, G. D., Kurty, R. and Pitcher, D., Electrical conductivity studies over a tectonically active area in eastern Canada, *J. Geomag. Geoelectr.* , v. 26, 125-146, 1974.

Banks, R. J., Data processing and interpretation in geomagnetic deep sounding, *Phys. Earth Planet Interiors*, v. 7,   339-348, 1973.

Beamish, D., The mapping of induced currents around the Kenya Rift: a comparison of techniques, *Geophys. J. R. ast. Soc.,* , 311-332, 1987

Beamish, D., A simple function for mapping induced currents, *Geophys. J. R. ast. Soc.* , 485-493, 1987

Chen, P. R. and Fung, P. C. W., Significance of the sign changing ofthe imaginary arrows in geomagnetic induction investigation, *Geophy. J. R. astr. Soc.*, v. 80, 257-263, 1985

Dawson, T. W., and Weaver, J. T., Three-dimensional induction in a non-uniform thin sheet at the surface of a uniformly conducting earth, *Geophys. J. R. astr. Soc.* , v. 59, 445-462, 1979

Dickinson, W. R., and W. S. Snyder, Geometry of subducted slabs related to San Andreas transform, *J. Geophys. Res.* , v. 84, 561-572, 1979.

Dvorak, Z., Electrical conductivity of several samples of olivinites, peridotites and dunites as a function of pressure and temperature, *Geophysics* , v. 38, 14-24, 1973.

Egbert, G. D., and J. R. Booker, Robust estimation of geomagnetic transfer functions, *Geophys. J. R. Astr. Soc.* , v. 87, 173-194, 1986.

Everett, J. E. and Hyndman, R. D. Geomagnetic variations and electrical conductivity

structure in south-western Australia, *Phys. Earth Planet. Interiors*, v. 1, 24-34, 1967

Fischer, G., Electromagnetic Induction Effects at an Ocean Coast, *Proc. of the IEEE*, v. 67 no. 7, 1050-1059, 1979

Green, V. R. and Weaver, J. T. Two-dimensional induction in a thin sheet of variable integrated conductivity at the surface of a uniformly conducting earth *Geophys. J. R. astr. soc.*, v. 55, 721 -736, 1978

Harwood, D. S., and Helley, E. J., Late Cenozoic Techonism of the Sacramento Valley, California, *U. S. Geological Survey Professional Paper 1359*, 9-12, 1987.

Helferty, M. G., Booker, J. R., Weertman, B. R., Auld, D. R. Detection of the southern edge of the subducted Gorda plate by geomagnetic induction *EOS, AGU Transactions*, v. 67 no. 44, 1225, 1986

Hensel, E. G., Delineation of a Channeled Current in Western Washington *M. Sci. Thesis*, Univ. of Wash. 1982

Isherwood, W. F., Geophysical Overview of the Geysers *U. S. Geol. Survey Prof. Paper 1141*, 83-95, 1981

Jachens, R. C., and A. Griscom, Three-dimensional geometry of the Gorda Plate beneath Northern California, *J. Geophys. Res.*, v. 88, 9375-9392, 1983.

Jones, A. R., The problem of current channeling, a critical review, *Geophys. Surv.*, v. 6, 79-122, 1983.

Kaufman, A. A., and Keller, G. V., *The Magnetotelluric Sounding Method*, Elsevier (New York, 1981) p. 564-571

Klein, D.P., Larsen, J. C., Magnetic induction fields (2-30 cpd) on Hawaii Island and their

implications regarding electrical conductivity in the oceanic mantle, *Geophys. J. R. astr. Soc.,* , v. 53, 61-77, 1984

Kurtz R. D., DeLaurier, J. M., and J. C. Gupta A magnetotelluric sounding across Vancouver Island, detects the subducting Juan de Fuca plate, *Nature* , v. 32, 1596-599, 1986.

Lachenbruch, A. H., and J. H. Sass, Heat flow and energetics of the San Andreas fault zone, *J. Geophys. Res* , v. 85, 6185-6222, 1980.

Law, L. D., Auld, D. R., and Booker, J. R. A geomagnetic variation anomaly coincident with the Cascade volcanic belt *J. Geophys. Res*, v. 85 no. B10, 5297-5302, 1980

McKurdy, D. McA., and Weaver, J. T., Induction in a thin sheet of variable conductance at the surface of a stratified earth-I. Two-dimensional theory *Geophys. J. R. astr. Soc.* , v. 78, 93-103, 1984

McKurdy, D. McA., and Weaver, J. T., Induction in a thin sheet of variable conductance at the surface of a stratified earth-II. Three-dimensional theory *Geophys. J. R. astr. Soc.* , v. 80, 177-194, 1985

Morin, F.J., Oliver, J. R., and Housley, R. M., Electrical properties of forsterite, Part II, *Phys. Rev. B.* , v. 19, 4434-4445, 1979

Parkhomenko, E. I., B. P. Belikov, and E. Dvorzhak, Influence of serpentinization upon the elastic and electrical properties of rocks, *Physics of the Solid Earth* (English Translation), No. 8, 551-556, 1973.

Parks, S. K., Distortion of magnetotelluric sounding curves by three-dimensional structures, *Geophysics* v. 50, 785-797, 1985

Price, Albert, T., The Theory of Geomagnetic Induction *Physics of the Earth and Planetary Interiors*, v. 7, 227-233, 1973

Ranganayaki, R. P., and Madden, T. R., Generalized thin sheet analysis in magnetotellurics: an extension of Price's analysis *Geophys. J. R. Astr. Soc.*, v. 60, 4445-457, 1980

Schmucker, U., Anomalies of geomagnetic variations in the southwestern United States, *Bull. Scripps Inst. Oceanog.* , v. 13, 1-165, 1970.

Schmucker, U., Regional induction studies: a review of methods and results, *Phys. of the Earth & Plan. Int.* , v. 7, 365-378, 1973

Shankland, T. J., Electrical Conduction in Mantle Materials *Evolution of the Earth; Geodynamics series*, v.5, 256-262

Silver, E. A., Transitional tectonics and Late Cenozoic structure of the continental margin off Northernmost California, *Geol. Soc. Am. Bull.* , v. 82, 1-22, 1971.

Stanley, W.D., Lackson, D.B., and Hearn, B.C., Preliminary results of geoelectrical investigations near Clear Lake, California *U. S. Geol. Survey Open-File Report*, 1973

Walter, S.R., Intermediate focus earthquakes associated with the Gorda Plate subduction in northern California., *Bull. Seism. Soc. Am.* , v. 75,583-588, 1986.

Weaver, J. T., Electromagnetic induction in thin sheet conductivity anomolies at the surface of the Earth, *Proc. of the IEEE,* v. 67 no 7, 1044-1049

Weaver, J. T., Regional induction in Scotland: an example of three- dimensional modelling using the thin sheet approximation, *Phys. Earth Plan. Interiors*, v. 28, 161-180, 1982

Wannamaker, P. E., Hohmann, G.W. and Ward, S. H., Magnetotelluric responses of three-dimensional bodies in layered earths, *Geophysics* , v. 51, 1517-1533, 1984

Zandt, G and K.P. Furlong, Evolution and thickness of the lithosphere beneath coastal California, *Geology* , v. 10, 376-381, 1982.